

# The seasonal cycle of satellite chlorophyll fluorescence observations and its relationship to vegetation phenology and ecosystem atmosphere carbon exchange



J. Joiner<sup>a</sup>, Y. Yoshida<sup>b</sup>, A.P. Vasilkov<sup>b</sup>, K. Schaefer<sup>c</sup>, M. Jung<sup>d</sup>, L. Guanter<sup>e</sup>, Y. Zhang<sup>e</sup>, S. Garrity<sup>f,\*</sup>, E.M. Middleton<sup>a</sup>, K.F. Huemmrich<sup>g</sup>, L. Gu<sup>h</sup>, L. Belli Marchesini<sup>i</sup>

<sup>a</sup> NASA Goddard Space Flight Center, Greenbelt, MD, USA

<sup>b</sup> Science Systems and Applications, Inc., Lanham, MD, USA

<sup>c</sup> National Snow and Ice Data Center, University of Colorado, Boulder, CO, USA

<sup>d</sup> Max Planck Institute for Biogeochemistry, Jena, Germany

<sup>e</sup> Free University of Berlin, Berlin, Germany

<sup>f</sup> Los Alamos National Laboratory, Los Alamos, NM, USA

<sup>g</sup> University of Maryland, Baltimore County, Joint Center for Environmental Technology (UMBC-JCET), Baltimore, MD, USA

<sup>h</sup> Environmental Sciences Division, Oak Ridge National Laboratory, Oak Ridge, TN, USA

<sup>i</sup> Vrije Universiteit, Amsterdam, The Netherlands

## ARTICLE INFO

### Article history:

Received 13 February 2014

Received in revised form 28 May 2014

Accepted 29 June 2014

Available online xxxx

### Keywords:

Fluorescence

Vegetation

Fluorescence

Chlorophyll

GOME-2

Gross primary productivity

Light-use efficiency

Flux tower

Growing season

Carbon uptake period

Phenology

## ABSTRACT

Mapping of terrestrial chlorophyll fluorescence from space has shown potential for providing global measurements related to gross primary productivity (GPP). In particular, space-based fluorescence may provide information on the length of the carbon uptake period. Here, for the first time we test the ability of satellite fluorescence retrievals to track seasonal cycle of photosynthesis as estimated from a diverse set of tower gas exchange measurements from around the world. The satellite fluorescence retrievals are obtained using new observations near the 740 nm emission feature from the Global Ozone Monitoring Experiment 2 (GOME-2) instrument offering the highest temporal and spatial resolution of available global measurements. Because GOME-2 has a large ground footprint ( $\sim 40 \times 80 \text{ km}^2$ ) as compared with that of the flux towers and the GOME-2 data require averaging to reduce random errors, we additionally compare with seasonal cycles of upscaled GPP estimated from a machine learning approach averaged over the same temporal and spatial domain as the satellite data surrounding the tower locations. We also examine the seasonality of absorbed photosynthetically-active radiation (APAR) estimated from satellite measurements. Finally, to assess whether global vegetation models may benefit from the satellite fluorescence retrievals through validation or additional constraints, we examine seasonal cycles of GPP as produced from an ensemble of vegetation models. Several of the data-driven models rely on satellite reflectance-based vegetation parameters to derive estimates of APAR that are used to compute GPP. For forested (especially deciduous broadleaf and mixed forests) and cropland sites, the GOME-2 fluorescence data track the spring onset and autumn shutoff of photosynthesis as delineated by the upscaled GPP estimates. In contrast, the reflectance-based indicators and many of the models, particularly those driven by data, tend to overestimate the length of the photosynthetically-active period for these biomes. Satellite fluorescence measurements therefore show potential for improving the seasonal dependence of photosynthesis simulated by global models at similar spatial scales.

© 2014 Elsevier Inc. All rights reserved.

## 1. Introduction

Vegetation phenology, the study of the timing and length of the terrestrial growing season and its connection to climate, has shown important relationships with climate change, surface meteorology, and the carbon cycle; it influences both spatial and temporal variability

in ecosystem productivity (Gu et al., 2003; White & Nemani, 2003; Churkina, Schimel, Braswell, & Xiao, 2005; Piao et al., 2008; Gu et al., 2009; Richardson et al., 2009, 2010, 2012). For example, the timing of leaf out, particularly for deciduous forests, is an important indicator of responses to climate change. It has major implications for the seasonal variation of numerous interactions between the biosphere and atmosphere including the partitioning of available energy into sensible and latent heat exchange as well as impacts to surface radiation budgets and dynamics (Randerson, Field, Fung, & Tans, 1999; Baldocchi et al., 2004; Churkina et al., 2005). The duration of the carbon uptake period

\* Corresponding author at: Pullman, WA, USA.

E-mail address: [Joanna.Joiner@nasa.gov](mailto:Joanna.Joiner@nasa.gov) (J. Joiner).

<sup>1</sup> Now at Decagon Devices.

(CUP), controlled by leaf out and senescence, can explain 80% of the spatial variance in annual net carbon exchange of ecosystems (NEE), defined as the amount of carbon entering and leaving an ecosystem (Baldocchi et al., 2001). Bauerle et al. (2012) have shown that while temperature is an important driver of seasonal changes in photosynthetic physiology, photoperiod also regulates leaf activity, particularly following summer solstice. They further show that proper accounting for this effect can significantly improve predictions of seasonal variations in atmospheric CO<sub>2</sub> within a global carbon-cycle model.

Several studies in North American forests (Richardson et al., 2009, 2010; Dragoni et al., 2010) show that earlier spring onset consistently results in higher gross ecosystem photosynthesis (GEP), as well as smaller increases in ecosystem respiration, leading to increased net ecosystem productivity (NEP) for both spring and annual flux integrals. Piao et al. (2008) find that autumnal warming produces increases in both photosynthesis and respiration, with greater increases in respiration. Dragoni et al. (2010) further show that in a North American deciduous forested site, the sensitivity of the carbon cycle to climate variability depends on the timing of the climate change with respect to phenological stages as well as to its sign and magnitude.

Terrestrial biosphere models have a large spread in the magnitude of predicted gross primary productivity (GPP) and show substantial differences in the temporal and biome-related (spatial) variability of GPP (Huntzinger et al., 2012). They show generally poor performance as compared with flux tower GPP estimates (Schaefer et al., 2012) and consistently predict that the growing season begins too early and ends late for deciduous forests; this results in an over-prediction of gross ecosystem photosynthesis during spring and autumn (Richardson et al., 2012). There is need for additional data to validate and improve these models.

The CUP and other phenological indicators have been estimated using satellite vegetation indices such as the Normalized Differential Vegetation Index (NDVI) and the Enhanced Vegetation Index (EVI) (e.g., Churkina et al., 2005; Ma et al., 2013; Zhang et al., 2003; Zhou et al., 2001). These indices have also been used within parameterized models to estimate gross primary productivity (GPP), defined as the total amount of carbon dioxide taken up from the atmosphere via photosynthesis (e.g., Running et al., 2004; Wang, Xiao, & Yan, 2010; Xiao et al., 2008). Many of these estimates are based on the light-use efficiency (LUE) model (Monteith, 1972) given by

$$GPP(t) = LUE(t) \times fPAR_{chl}(t) \times PAR_{chl}(t) = LUE(t) \times APAR_{chl}(t), \quad (1)$$

where  $fPAR_{chl}$  is the fractional absorbed (by chlorophyll) photosynthetically-active radiation ( $PAR_{chl}$ ), LUE is defined as the amount of carbon a specific vegetation type can fix biochemically per unit of absorbed solar energy,  $APAR_{chl}$  is the absorbed PAR (for convenience the subscript 'chl' is henceforth dropped), and  $t$  is time. For example, satellite reflectance-based  $fPAR$  estimates are given in the MOD15A2 product from the MODerate-resolution Imaging Spectroradiometer (MODIS), and LUE can be parameterized as a function of meteorological parameters for a given biome. However, the use of reflectance-based indicators such as  $fPAR$  can be problematic in areas where vegetation indices do not drop when vegetation stays green while photosynthesis declines, (e.g., in evergreen needleleaf forests), in regions affected by seasonal snow cover under the canopy, and possibly in areas with high heterogeneity within a satellite pixel (e.g., Churkina et al., 2005; Xiao et al., 2004). In these cases, LUE models must rely more heavily on their LUE parameterizations.

Fluorescence measurements, particularly global observations from space, offer an alternative means of remotely sensing the functional status of vegetation. Fluorescence is generated during the photosynthetic process. The excitation for chlorophyll fluorescence in nature is provided by sunlight. The broad-band emission has two chlorophyll-related peaks at red and far-red wavelengths near 685 and 740 nm, respectively (e.g., Campbell, Middleton, Corp, & Kim, 2008; Corp et al., 2003).

At the canopy level, steady-state fluorescence from chlorophyll in vegetation at emission wavelength  $\lambda_{em} = 740$  nm, henceforth denoted  $F_{740}$ , in general can be expressed as an integral of contributions over all excitation wavelengths from ultraviolet to near-infrared wavelengths, i.e.,

$$F_{740}(t) = e(\lambda_{em} = 740 \text{ nm}, t) \int_{\lambda_{ex}} \Theta_F(\lambda_{ex}, \lambda_{em}, t) fPAR_F(\lambda_{ex}, t) I(\lambda_{ex}, t) d\lambda_{ex}, \quad (2)$$

where  $\lambda_{ex}$  is the excitation wavelength,  $I$  is incident radiation at the surface,  $e$  is the fractional amount of fluorescence that escapes the canopy, and  $\Theta_F$  is the fluorescence efficiency. Here it is recognized (by use of the subscript F) that  $fPAR$  for chlorophyll fluorescence ( $fPAR_F$ ) may differ slightly from  $fPAR$  for photosynthesis ( $fPAR_{chl}$ ).  $fPAR_F$  and  $e$  are determined by canopy structure and vegetation biochemistry, captured in spectral optical properties.

A more simplified formulation has also been used to express steady state fluorescence (e.g., Berry et al., 2013; Louis et al., 2005), i.e.,

$$F_{740}(t) \approx e(t) \Theta_F(t) \times fPAR_F(t) \times PAR_F(t) = e(t) \Theta_F(t) \times APAR_F(t). \quad (3)$$

Again, we recognize that  $PAR_F$  may differ somewhat from  $PAR_{chl}$  (typically assumed to be 400–700 nm) as the action spectrum for fluorescence may weight ultraviolet wavelengths more heavily (Chappelle & Williams, 1987; Middleton, Corp, & Campbell, 2008; Rosema, Verhoef, Schoote, & Snel, 1991). Eq. (3) is similar in form to Eq. (1). Conversely, Eq. (1) could also be written in a somewhat more complex form similar to Eq. (2) as an integral over photosynthetically-active wavelengths. Eq. (3) may be used to approximate Eq. (2) provided that the spectral structure of  $\Theta_F$ ,  $fPAR_F$ , and  $I$  remains relatively constant with time.

If Eq. (3) is taken as is and  $APAR_F(t) \approx APAR_{chl}(t)$ , then the ratio of  $GPP(t)$  to  $F_{740}(t)$  is proportional to the ratio of LUE(t) to  $e(t)\Theta_F(t)$ . There is theoretical evidence to support that under strong illumination, the ratio of LUE to  $\Theta_F$  remains relatively constant, at least for fluorescence from photosystem II (Berry et al., 2013). Experimental studies have also shown that in high light conditions (i.e., in the early afternoon and late morning when many satellite measurements are made), chlorophyll fluorescence is positively correlated with  $APAR$ , LUE, and GPP (e.g., Amoros-Lopez et al., 2008; Flexas et al., 2002; Guanter et al., 2014; Louis et al., 2005; Meroni et al., 2008; van der Tol, Verhoef, & Rosema, 2009; Zarco-Tejada et al., 2009). Therefore, we may expect similar seasonal variability in GPP and  $F_{740}$  for a given vegetation type as long as  $e$  remains relatively constant.

The main objective of this study is to test the ability of  $F_{740}$  to accurately track the seasonal cycle of GPP across different vegetation types. A new  $F_{740}$  data set derived from observations from the GOME-2 satellite instrument provides the temporal and spatial resolution needed for a first direct comparison with global flux tower gas exchange measurements in terms of the seasonality of photosynthesis. Towards our goal, we compare the seasonal cycle of GOME-2  $F_{740}$ , averaged over multiple years, with that of GPP from a diverse set of flux towers from around the world at middle latitudes where there is a distinct cycle in photosynthesis. Because the spatial scale of the tower measurements is much smaller than the large footprint GOME-2 satellite measurements (additionally averaged over time and space to reduce random errors), we also compare with upscaled GPP estimated with the Max Planck Institute for Biogeochemistry (MPI-BGC) machine learning algorithm; these upscaled GPP estimates are averaged at the same spatial resolution and over the same time period as the GOME-2  $F_{740}$  retrievals. This allows us to assess potential representativeness errors in the comparison between GOME-2  $F_{740}$  and GPP from flux towers. We perform additional comparisons to determine whether the seasonal cycle of fluorescence more closely tracks photosynthesis as compared with absorbed photosynthetically-active radiation (APAR),

derived from satellite reflectances. Finally, in order to assess whether fluorescence data may provide additional validation of and/or constraints for global vegetation models, we compare seasonal cycles of GOME-2  $F_{740}$  and GPP generated from an ensemble of state-of-the-art physically-based and data driven models; the mostly global models are typically run at similar spatial resolutions as compared with the GOME-2  $F_{740}$  data set.

## 2. Data

### 2.1. GOME-2 fluorescence at 740 nm ( $F_{740}$ )

#### 2.1.1. Background on remote sensing of terrestrial chlorophyll fluorescence

Fluorescence from chlorophyll in terrestrial vegetation has been measured with ground-, aircraft, and satellite-based instrumentation at wavelengths in and surrounding the O<sub>2</sub> A- and B-bands (e.g., Amoros-Lopez et al., 2008; Guanter et al., 2007, 2013; Meroni et al., 2009; Middleton et al., 2010; Moya et al., 2004; Rascher et al., 2009). The filling-in of solar Fraunhofer lines by terrestrial fluorescence at wavelengths on both shoulders of the O<sub>2</sub>-A absorption band (755 and 770 nm) has been observed using the Japanese Greenhouse gases Observing SATellite (GOSAT) (Frankenberg et al., 2011, Guanter et al., 2012; Joiner et al., 2011, 2012). Joiner et al. (2012) found a small filling-in of the broad solar Fraunhofer ionized calcium (Ca II) line at 866 nm consistent with fluorescence using the SCanning Imaging Absorption spectrometer for Atmospheric CHartographY (SCIAMACHY) instrument flying on the European Space Agency's (ESA's) EnviSat.

Joiner et al. (2013) demonstrated that fluorescence can be retrieved near the 740 nm emission peak using atmospheric hyperspectral satellite-based instrumentation. They applied their approach to data from the Global Ozone Monitoring Experiment 2 (GOME-2) flying on operational European meteorological (MetOp) satellites. GOME-2 provides the highest fidelity satellite fluorescence data set currently available; the data, gridded to a spatial resolution of about 0.5° latitude by 0.5° longitude at a monthly time resolution, have estimated errors of 0.1–0.4 mW/m<sup>2</sup>/nm/sr.

#### 2.1.2. The GOME-2 instrument

GOME-2 is a grating spectrometer that measures backscattered sunlight in a nadir-viewing geometry at wavelengths between 270 and 800 nm in four separate channels (Munro et al., 2006). It has been launched on the MetOp A and B platforms on 19 October 2006 and 17 September 2012, respectively. Both MetOp A and B are in sun-synchronous orbits with an equator crossing time near 09:30 AM, but approximately 45 min (half an orbit) apart.

Here, we use data from MetOp A covering 2007–2011. We use radiances from channel 4 at a spectral resolution of ~0.5 nm with a signal-to-noise ratio of ~1000. The nominal ground pixel lengths at nadir are approximately 40 and 80 km in the along- and across-track directions, respectively. The default swath width is 1920 km. This enables global coverage of the Earth's surface within about 1.5 days. The actual coverage for fluorescence retrievals is reduced because data in heavily clouded overcast conditions are filtered out as described in more detail below.

#### 2.1.3. Retrieval of far-red fluorescence from GOME-2

We derive GOME-2  $F_{740}$  primarily from the filling-in of solar Fraunhofer lines in the vicinity of the 740 nm far-red fluorescence emission peak as in Joiner et al. (2013). The basis for the retrieval relies on the fact that an additive signal such as fluorescence produces a filling-in of a solar line when an Earth backscattered spectrum is normalized with respect to the solar spectrum or a reference spectrum that does not contain fluorescence. The retrieval uses a principal component analysis approach with a simplified radiative transfer model to disentangle the spectral signatures of three basic components: atmospheric absorption, surface reflectance, and fluorescence emission. GOME-2  $F_{740}$  is given in

radiance units (mW/m<sup>2</sup>/nm/sr) and varies somewhat with viewing geometry (Guanter et al., 2012; Joiner et al., 2012).

The retrieval algorithm performed well when tested with simulated data and was applied to radiances from GOME-2 (Joiner et al., 2013). Fluorescence from GOME-2 compared well in terms of spatial and temporal variability with that from GOSAT (Guanter et al., 2012) obtained with a more simple retrieval approach. The GOME-2 fluorescence data set provides substantially improved sampling and precision (and therefore spatial resolution) as compared with GOSAT; therefore only GOME-2 data are used in this study.

We have made some minor changes to the approach of Joiner et al. (2013) that bring the GOME-2 results into slightly better agreement with GOSAT and reduce small biases where no fluorescence is expected. We use a spectral fitting window between 715 and 758 nm and a single set of principal components (PCs), derived from cloudy data over ocean, to estimate the spectral structure of atmospheric absorption; absorption is dominated by water vapor over this spectral range. The O<sub>2</sub> A-band is not included in the fitting window. The principal components are derived from radiance spectra here as opposed to the logarithm of the radiance spectra as in Joiner et al. (2013). We also attempted to correct for drift in the absolute instrument calibration by fitting a degradation factor to the GOME-2 solar spectra.

#### 2.1.4. Processing of GOME-2 fluorescence retrievals

For cloud screening of GOME-2 data as in Joiner et al. (2013), we make use of the concept of the effective cloud fraction,  $f_e$ , described in detail by Stammes et al. (2008).  $f_e$  can be computed by inverting the following equation:

$$I_m = I_{\text{clr}}(1 - f_e) + I_{\text{cld}}f_e, \quad (4)$$

where  $I_m$  is the measured radiance, and  $I_{\text{clr}}$  and  $I_{\text{cld}}$  are considered to be clear and cloudy subpixels (i.e., the independent pixel approximation).  $I_{\text{clr}}$  is computed using a surface albedo data set as described in Joiner et al. (2013) and  $I_{\text{cld}}$  is modeled as a Lambertian surface with an effective reflectivity of 0.8. In this mixed Lambertian model of cloudy scenes,  $f_e$  is not a true geometrical cloud fraction, but rather represents an estimated fraction of the surface that is completely shielded by clouds (i.e., the satellite sensor sees only the clear fraction of a pixel approximated by  $1 - f_e$ ).

Here, we retain only pixels with  $f_e < 40\%$ . The impact of this empirically chosen threshold is described in more detail in Section 3. Due to uncertainties in the GOME-2 absolute calibration and the surface albedo data set used in the calculation of  $f_e$ , our cloud screening procedure primarily removes heavily clouded (overcast) pixels; cases of thin and broken clouds are retained in the sample. Clouds do not affect the spectral signature of fluorescence as is the case for vegetation indices derived from satellite reflectances. Therefore, the main effect of clouds on fluorescence measurements is a shielding effect, i.e., a fraction of the surface is shielded by clouds/aerosol from satellite observation. Radiative transfer simulations show that a substantial fraction of the fluorescence signal (~80%) can penetrate through clouds/aerosols of low to moderate optical thickness (up to 5) (Frankenberg, O'Dell, Guanter, & McDuffie, 2012). Joiner et al. (2012) similarly estimate that with a 40% geometrical cloud cover, 80% or more of the surface will be seen for cloud optical thicknesses up to 10.

We generate climatological 8 day mean GOME-2  $F_{740}$  values using GOME-2 data averaged over the time period Jan. 2007 through Dec. 2011. The 8-day intervals were chosen to match those of the MODIS fPAR (MOD15) data set as described below. For comparison with data from a given flux tower site, we average quality-controlled pixels that have centers within 1° latitude and 1° longitude of the tower location; we apply quality control checks as described in Joiner et al. (2013). In addition, we use only GOME-2 pixels with solar zenith angles (SZA) less than 70° to avoid possible biases due to rotational-Raman scattering (Vasilkov, Joiner, & Spurr, 2013).

**Table 1**  
Network sites used in analysis (see text for more details).

| Code   | State/country & name                     | Years     | IGBP <sup>a</sup> | IGBP <sup>b</sup> | %    | Reference   |
|--------|--|-----------|-------------------|-------------------|------|---|
| AU-Fog | Fogg Dam, Australia                      | 2006–2007 | WET               | SAV               | 72.2 | Beringer, Livesley, Randle, and Hutley (2013), Ma et al. (2013)                                 |
| AU-How | Howard Springs, Australia                | 2001–2006 | WSA               | SAV               | 61.1 | Beringer et al. (2011), Ma et al. (2013)  |
| AU-Tum | Tumbarumba, Australia                    | 2001–2006 | EBF               | EBF               | 41.0 | Bonan et al. (2011)   |
| AU-Wac | Wallaby Creek, Australia                 | 2005–2007 | EBF               | EBF               | 43.8 | Kilinc, Beringer, Hutley, Tapper, and McGuire (2013)  |
| BW-Ma1 | Maun–Mopane Woodland, Botswana           | 1999–2001 | WSA               | SAV               | 91.0 | Veenendaal, Kolle, and Lloyd (2004)   |
| CA-Mer | Quebec Eastern Peatland–Mer Bleue        | 1998–2005 | WET               | DBF               | 70.1 | Lafleur, Roulet, and Admiral (2001), Kross (2011)   |
| CA-Qcu | Quebec Boreal Cutover Site               | 2001–2007 | ENF               | ENF               | 72.2 | Giasson, Coursolle, and Margolis (2006)   |
| DE-Tha | Anchor Station Tharandt, Germany         | 1996–2007 | ENF               | MF                | 67.4 | Grünwald and Bernhofer (2007)   |
| IL-Yat | Yatir, Israel                            | 2001–2006 | ENF               | SH                | 45.1 | Rotenberg and Yakir (2010)  |
| IT-Amp | Amplero, Italy                           | 2002–2006 | GRA               | MF                | 67.4 | Gilmanov et al. (2010)  |
| IT-Cpz | Castelporziano, Italy                    | 1997–2007 | EBF               | WAT               | 45.1 | Garbulsky, Penuelas, Papale, and Filella (2008)   |
| IT-Ro1 | Roccarespampani, Italy                   | 2000–2007 | DBF               | MF                | 53.5 | Migliavacca et al. (2010)   |
| NL-Hor | Horstermeer, Netherlands                 | 2004–2007 | GRA               | CRO               | 54.9 | Hendriks, van Huissteden, Dolman, and van der Molen (2007, 2008)                                |
| NL-Loo | Loobos, Netherlands                      | 1996–2007 | ENF               | CRO               | 48.6 | Elbers, Jacobs, Kruijt, Jans, and Moors (2011)  |
| US-ARM | OK ARM Southern Great Plains–Lamont      | 2000–2007 | CRO               | GRA               | 44.4 | Billesbach, Fischer, Torn, and Berry (2004)   |
| US-Aud | AZ Audubon Research Ranch                | 2002–2006 | GRA               | SAV               | 47.2 | Gilmanov et al. (2010)  |
| US-Bar | NH Bartlett Experimental Forest          | 2004–2006 | DBF               | DBF               | 70.1 | Jenkins et al. (2007)   |
| US-Bkg | SD Brookings                             | 2004–2006 | GRA               | CRO               | 79.2 | Gilmanov et al. (2005)  |
| US-Blo | CA Blodgett Forest                       | 1997–2007 | ENF               | ENF               | 53.5 | Goldstein et al. (2000)   |
| US-Bo1 | IL Bondville                             | 1996–2007 | CRO               | CRO               | 77.1 | Turner, Urbansky et al. (2003)  |
| US-Dk3 | NC Duke Forest Loblolly Pine             | 1998–2005 | ENF               | MF                | 45.8 | Luo et al. (2001), Stoy et al. (2008)   |
| US-FPe | MT Fort Peck                             | 2000–2006 | GRA               | GRA               | 66.7 | Gilmanov et al. (2003)  |
| US-Goo | MS Goodwin Creek                         | 2002–2006 | GRA               | DBF               | 50.0 | Yuan et al. (2007)  |
| US-Ha1 | MA Harvard Forest EMS Tower (HFR1)       | 1991–2006 | DBF               | DBF               | 97.2 | Urbanski et al. (2007), Goulden, Munger, Fan, Daube, and Wofsy (1996)                           |
| US-Ho1 | ME Howland Forest (main tower)           | 1996–2004 | ENF               | MF                | 61.8 | Thornton et al. (2002)  |
| US-Ho2 | ME Howland Forest (west tower)           | 1999–2005 | ENF               | MF                | 61.8 | Thornton et al. (2002)  |
| US-IB1 | IL Fermi Agricultural                    | 2005–2007 | CRO               | CRO               | 50.7 | Xiao et al. (2008)  |
| US-IB2 | IL Fermi Prairie                         | 2004–2007 | GRA               | CRO               | 50.7 | Xiao et al. (2008)  |
| US-Los | WI Lost Creek                            | 2000–2006 | CSH               | MF                | 92.4 | Sulman, Desai, Cook, Saliendra, and Mackay (2009), Desai et al. (2008)                          |
| US-MMS | IN Morgan Monroe State Forest            | 1999–2006 | DBF               | MF                | 37.5 | Schmid, Grimmer, Cropley, Offerle, and Su (2000), Dragoni, Schmid, Grimmer, and Loescher (2007) |
| US-MOz | MO Missouri Ozark Site                   | 2004–2007 | DBF               | DBF               | 59.7 | Gu et al. (2003, 2006, 2012)  |
| US-Me2 | OR Metolius Intermed. Pine               | 2002–2007 | ENF               | ENF               | 56.2 | Loescher et al. (2006)  |
| US-Me3 | OR Metolius Second Young Pine            | 2004–2005 | ENF               | ENF               | 56.2 | Loescher et al. (2006)  |
| US-Me4 | OR Metolius-old aged ponderosa pine      | 1996–2000 | ENF               | ENF               | 56.2 | Loescher et al. (2006)  |
| US-Me5 | OR Metolius First Young Pine             | 1999–2002 | ENF               | ENF               | 56.2 | Loescher et al. (2006)  |
| US-NR1 | CO Niwot Ridge                           | 1998–2007 | ENF               | ENF               | 41.0 | Monson et al. (2002)  |
| US-Ne1 | NE Mead – irrigated continuous maize     | 2001–2006 | CRO               | CRO               | 97.9 | Suyker, Verma, Burba, and Arkebauer (2005), Verma et al. (2005)                                 |
| US-Ne2 | NE Mead – irrigated maize–soybean rot.   | 2001–2006 | CRO               | CRO               | 97.9 | Suyker et al. (2005), Verma et al. (2005)   |
| US-Ne3 | NE Mead – rainfed maize–soybean rot.     | 2001–2006 | CRO               | CRO               | 98.6 | Suyker et al. (2005), Verma et al. (2005)   |
| US-Oho | OH Oak Openings                          | 2004–2005 | DBF               | CRO               | 69.4 | Sun et al. (2010)   |
| US-PFa | WI Park Falls/WLEF                       | 1995–2005 | MF                | MF                | 96.5 | Davis et al. (2003) Desai et al. (2008)   |
| US-SO2 | CA Shy Oaks Old                          | 1998–2006 | CSH               | SH                | 72.9 | Stylinski, Gamon, and Oechel (2002)   |
| US-SP1 | FL Slashpine–Austin Cary-65 yr nat regen | 2000–2006 | ENF               | MF                | 47.2 | Powell et al. (2008)  |
| US-SP2 | FL Slashpine–Mize-clearcut-3 yr regen    | 1998–2005 | ENF               | MF                | 47.2 | Bracho et al. (2012)  |
| US-SP3 | FL Slashpine–Donaldson-mid-rot-12 yr     | 1999–2005 | ENF               | MF                | 47.2 | Bracho et al. (2012)  |
| US-Shd | OK Shidler Tallgrass Prairie             | 1997–2000 | GRA               | GRA               | 44.4 | Gilmanov et al. (2003)  |
| US-Syv | MI Sylvania Wilderness Area              | 2001–2006 | MF                | MF                | 88.9 | Desai, Bolstad, Cook, Davis, and Carey (2005)   |
| US-Ton | CA Tonzi Ranch                           | 2001–2007 | WSA               | SAV               | 55.6 | Sims et al. (2005)  |
| US-UMB | MI Univ. Mich. Biological Station        | 1999–2006 | DBF               | MF                | 84.7 | Gough, Hardiman, Vogel, Nave, and Curtis (2010)   |
| US-Var | CA Vaira Ranch- Ione                     | 2000–2007 | GRA               | SAV               | 55.6 | Sims et al. (2005)  |
| US-WBW | TN Walker Branch Watershed               | 1995–2000 | DBF               | MF                | 49.3 | Misson et al. (2007)  |
| US-WCr | WI Willow Creek                          | 1998–2006 | DBF               | MF                | 99.3 | Cook et al. (2004)  |
| ZA-Kru | Skukuza–Kruger Natl. Park, South Africa  | 2001–2003 | SAV               | SAV               | 75.7 | Scholes et al. (2001)   |

<sup>a</sup> IGBP vegetation type at site — CRO: Croplands; CSH: Closed Shrublands; DBF: Deciduous Broadleaf Forest; EBF: Evergreen Broadleaf Forest; ENF: Evergreen Needleleaf Forest; GRA: Grasslands; GMF: Grass + Mixed Forest; MF: Mixed Forest; OSH: Open Shrublands; SAV: Savannas; SH: Shrublands; WET: Wetlands; WSA: Woody Savannas.

<sup>b</sup> Predominant IGBP type within satellite averaging area (see text) where WSA and SAV are combined as SAV, CSH and OSH as SH, and MF and GMF as MF.

We estimated uncertainties in each 8-day bin as the root sum square of the standard error of the mean (of all samples in the bin) and a nominal GOME-2  $F_{740}$  constant error of 0.2 mW/m<sup>2</sup>/nm/sr. The standard errors alone appear to underestimate the uncertainties as the large numbers of samples used in the averaging process lead to relatively small standard errors in most bins. The constant error is introduced to account for other error sources such as cloud contamination.

2.2. AmeriFlux and FluxNet tower measurements

We use quality-controlled 1/2 hourly GPP from the FluxNet synthesis project (<http://www.fluxdata.org/>) (Baldocchi et al., 2001) and additional US stations in the AmeriFlux site synthesis project (Barr, Ricciuto et al., 2013; Barr, Richardson et al., 2013). Table 1 provides tower station details including the starting and ending years of the observational record used here and the International Geosphere Biosphere Programme (IGBP) vegetation type at the station. Table 1 also lists the dominant vegetation type, according to an IGBP land cover map, corresponding to the area over which the GOME-2  $F_{740}$  data are averaged (within 1° latitude, 1° longitude of a station location), denoted IGBP<sub>avg</sub>. Here, we combined open and closed shrublands into a single type (shrublands), and woody savannas and savannas into one type (savannas). Our mixed forest type contains the IGBP type ‘grass + mixed forest’ in addition to ‘mixed forest’. We provide the approximate percentage (%) of the satellite-averaging box covered by the dominant vegetation type IGBP<sub>avg</sub> in Table 1. Fig. 1 displays locations and vegetation types in a mapped format.

We compute 8-day means of GPP estimated from the tower data in a manner similar to our processing of GOME-2 data. Each 8-day value is

an average over all available years for a particular tower. The 8-day intervals match those of the MOD15 data set. We do not include gap-filled data in our data processing. We use all available GPP data regardless of the cloud conditions and average data over all hours. We checked that the derived seasonal cycle of GPP does not change substantially if we use only data near the satellite overpass time.

For inclusion of a site in our analysis, at least 40 quality-controlled GOME-2 pixels must have been collected for a given 8 day period and at least 75% of the 8-day bins within the year must be filled. Unfortunately, the tower observational time records do not generally coincide with those of GOME-2. Therefore, we must compare seasonal cycles that have been averaged over different sets of years (for each site). This may produce some differences between the tower and other satellite data sets as there can be interannual variability, particularly in the initiation of photosynthesis (e.g., Gu et al., 2008). Comparisons of derived seasonal cycles of photosynthesis from flux towers and GOME-2 satellite data are considered to be climatological. By using averages over several years, we may smooth out some of the interannual variability.

Uncertainties in the GPP derived from flux tower measurements have been computed for the Ameriflux sites (Schaefer et al., 2012); total uncertainties include contributions from random errors, threshold friction velocity uncertainty, and partitioning uncertainty (owing to uncertainty in the estimated ecosystem respiration). The partitioning uncertainty is based on the variance produced by different partitioning algorithms (Desai et al., 2008). Random uncertainty is the largest contributor to the total uncertainties (50–90%).

Using the available Ameriflux data, we find that total uncertainties in the weekly-mean GPP ( $GPP_{weekly}$ ) varies with  $GPP_{weekly}$ . We fit a general exponential function to the Ameriflux data to approximate the weekly-averaged total GPP uncertainties ( $\sigma_{GPP_{tot}}$ ), i.e.,

$$\sigma_{GPP_{tot}} = 0.5085 * e^{0.1088 * GPP_{weekly}} \tag{5}$$

We then apply this formulation to all tower sites to approximate uncertainties in the derived 8-day GPP.

2.3. The MPI-BGC data-driven model of GPP

Estimates of GPP from the Max Planck Institute for Biogeochemistry (MPI-BGC) originate from upscaling a global dataset of eddy covariance based measurements (Jung et al., 2011). A machine learning algorithm (Model Tree Ensembles, MTE) as described by Jung, Reichstein, & Bondeau (2009) was trained to predict monthly observed GPP at the tower sites based on remotely sensed fPAR, climate, and vegetation type data. The trained model was then applied using spatial grids of the explanatory variables to generate global monthly GPP estimates at a 0.5° spatial resolution (see Jung et al., 2011, for details).

We averaged monthly MPI-BGC GPP estimates from Jan. 2007–Dec. 2011, the same time period used for GOME-2 data. We then averaged all gridboxes within 1° latitude and longitude of each flux tower location, the same spatial scale as represented by the GOME-2 data. We may then use the upscaled MPI-BGC GPP estimates to assess the effect of the different spatial scales of the flux tower and GOME-2 satellite data. We use Eq. (5) to estimate uncertainties in the upscaled GPP.

2.4. GPP model ensemble

We also examine seasonal cycles (weekly output) of GPP as produced by an ensemble of 24 models that were used in the study of Schaefer et al. (2012). MPI-BGC is not included in the ensemble. The models were driven with gap-filled meteorological data from each tower site. Other input parameters and biophysical characteristics

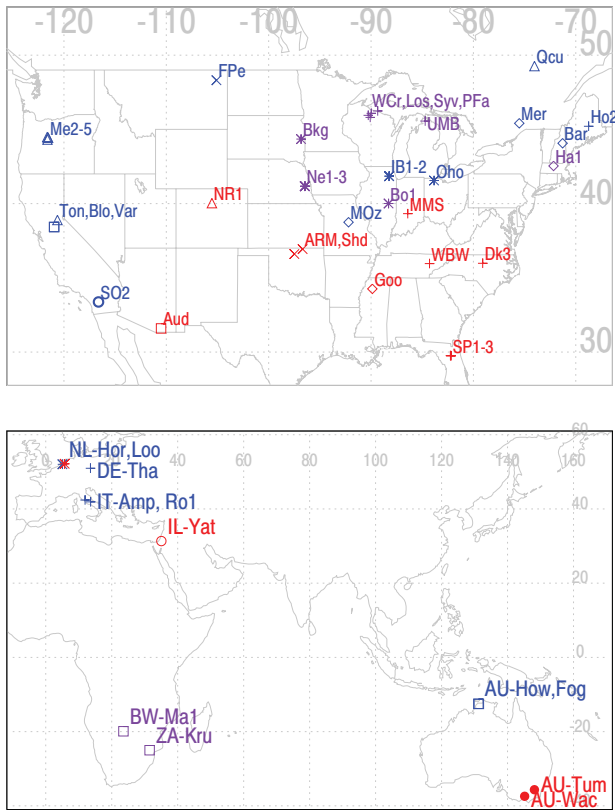


Fig. 1. Locations of flux towers and their designations used in this study; purple, blue, and red indicate that the primary vegetation type (IGBP) covers approximately 75–100%, 50–75%, and 0–50%, respectively, of the surrounding satellite averaging area; symbols show dominant vegetation type for the satellite averaging area; +: Mixed Forest (including ‘grass + MF’); \*: Croplands; x: Grasslands; ◊: Deciduous Broadleaf Forest; △: Evergreen Needleleaf Forest; square: Savannas (including woody); ○: Shrublands (open and closed); ●: Evergreen Broadleaf Forest. (For interpretation of the references to color in this figure legend, the reader is referred to the web version of this article.)

were derived from local observations as discussed in Schaefer et al. (2012).

The model ensemble includes 14 physically-based models that have prognostic phenology and 10 data-driven models that use remote sensing data to determine leaf area index (LAI) and/or GPP. The models were classified in Schaefer et al. (2012) as either enzyme-kinetic (EK) (17 models) or LUE (7) models. Both EK and LUE groupings include a combination of data-driven and physically-based approaches to estimate LAI and/or GPP. Because some of the models are targeted for a particular biome (e.g., forest or agriculture), not all of the models produced a simulation for a given site. Therefore, each site has a different model ensemble associated with it.

### 2.5. MODIS fPAR/APAR (MOD15)

We used 8-day means of the canopy fPAR derived from the Terra MODIS collection 5 (MOD15A2) (Myneni et al., 2002) obtained from the Oak Ridge National Laboratory's Distributed Active Archive Center (ORNL DAAC, 2010). We used quality controlled data averaged over approximately 7 km × 7 km regions centered on a flux tower. The original data are produced as an 8-day maximum value composite at 1 km spatial resolution. Because the MODIS data set is produced as a composite using maxima rather than means (as was done for the  $F_{740}$  and tower GPP data) and are then specified as a single value at the midpoint of the compositing period, it should be noted that the values may be weighted towards earlier dates in spring during the onset of greening (by up to ~4 days or half the compositing period) and similarly towards later dates in autumn as greenness is declining.

APAR values are computed using the MOD15A2 fPAR × cos( $\theta$ ), where  $\theta$  is the average solar zenith angle for each time period near the MetOp-A and Terra local overpass times; cos( $\theta$ ) is a proxy for the seasonal cycle of potential PAR. We compute a climatological seasonal cycle of APAR by averaging data for each 8-day interval over the time period Feb. 2000–Oct. 2011. The averaged data are then plotted at the midpoint of the time interval. We estimate uncertainties similar to what was done for GOME-2  $F_{740}$  as described above; for each 8-day bin, we estimate the uncertainty as the root sum square of the standard error of the mean (for each 8-day interval) and a nominal constant error of 0.03 intended to account for additional error sources such as cloud contamination and compositing effects.

## 3. Results and discussion

### 3.1. Seasonal variations in tower-based and upscaled GPP, MODIS-based APAR, and GOME-2 $F_{740}$

In this section, we assess the ability of GOME-2  $F_{740}$  to track the seasonality of photosynthesis as delineated by tower-based and upscaled GPP estimates. Figs. 2–3 show average seasonal cycles of GPP (normalized to unity at the maxima) from towers along with the upscaled GPP from MPI-BGC, GOME-2  $F_{740}$ , and MODIS-based estimates of APAR, for sites representing a variety of biomes. Similar plots for the other sites listed in Table 1 are provided in the Supplemental information (SI). All GOME-2 pixels with centers within 1° latitude and longitude of the flux tower site are averaged here, and similarly all MPI-BGC gridboxes within 1° latitude and longitude of the site are averaged. The GOME-2  $F_{740}$  and MPI-BGC GPP data are averaged over the same years (2007–2011). Therefore, we expect better agreement of GOME-2  $F_{740}$  with MPI-BGC GPP as compared with tower-based GPP due to the closer collocation in both time and space of GOME-2  $F_{740}$  with MPI-BGC GPP.

The tower data indicate a relatively short growing season for the agricultural Nebraska site US-Ne1 (Fig. 2a), composed of continuous maize crops. This short duration of photosynthesis is similarly shown by both GOME-2  $F_{740}$  and the upscaled MPI-BGC GPP estimates. The upscaled GPP and GOME-2  $F_{740}$  display a slightly wider mean growing season as compared with the tower-based GPP. This may be expected

as GOME-2  $F_{740}$  and the upscaled GPP estimates are analyzed at similar and larger spatial scales as compared with the tower measurements. The larger footprints of GOME-2  $F_{740}$  and MPI-BGC GPP likely contain contributions from different crops such as soybeans that have somewhat lengthier growing seasons and vegetation types other than croplands; this may explain the more gradual increases(decreases) in spring(autumn). It should be noted that monthly mean MPI-BGC GPP estimates are in excellent agreement with 8-day mean GOME-2  $F_{740}$ ; this indicates that monthly-mean values are adequate for the present analysis.

A significantly earlier springtime rise and later autumn decline is seen in MODIS-based APAR as compared with GOME-2  $F_{740}$  and the GPP estimates for the US-Ne1 agricultural site and similarly for the agricultural US-IB1 site (see SI). The later decline in autumn may be expected as APAR does not contain information about LUE and therefore may remain high in the presence of green vegetation that is not engaging in photosynthesis. However, the almost symmetrical early rise in spring is more difficult to explain as green vegetation in spring should be photosynthetically-active.

One explanation is that the reflectances used to generate MODIS (MOD15) fPAR are sensitive to pigments in vegetation and soil other than chlorophyll. It has been shown that the MOD15 estimate of fPAR applies to the whole vegetation canopy, both photosynthetic and nonphotosynthetic components, and does not provide consistent relationships to photosynthetic processes at the ecosystem scale (Turner, Ritts et al., 2003; Turner, Urbansky et al., 2003; Turner et al., 2006; Zhang et al., 2009). Alternative methods have emerged to improve estimates of fPAR related to only the photosynthetic component (see Zhang, Middleton, Cheng, & Landis, 2013, and references therein). One such approach involves the retrieval of a new fPAR parameter related only to the chlorophyll-containing foliage (called fPAR<sub>chl</sub>) (Zhang et al., 2005, 2006, 2009; Zhang, Middleton, Gao, & Cheng, 2012). This parameter shows a seasonal cycle more consistent with tower-based GPP for several tower sites used in our study including the agricultural sites US-Ne2 and US-Ne3, and a deciduous broadleaf forest site (US-Bar) (Cheng, Zhang, Lyapustin, Wang, & Middleton, 2014).

The MODIS-based APAR also shows a slightly earlier spring onset of activity for the northern deciduous broadleaf forest (DBF) and mixed-forest (MF) sites (US-UMB and US-Ha1) in Fig. 2b and c, respectively, and is lagged in the autumn decline with respect to the tower GPP at these sites. We note that MODIS fPAR typically stays above 0.2 throughout the year for these sites. For some sites such as US-Ha1, fPAR remains very high (~0.5) throughout the winter, possibly owing to contributions from evergreen needleleaf vegetation or other pigments in the woody parts of the vegetation. While multiplication of fPAR by the PAR-proxy brings MODIS-based APAR to near zero in winter, GOME-2  $F_{740}$  minimum winter values are at or closer to zero. MODIS-based APAR shows a much closer relationship with tower-based GPP at the more southern US-Dk3 site (Fig. 2d) where GPP does not drop to zero in winter.

GOME-2  $F_{740}$  tracks the sharp springtime rise and autumn drop in GPP, as shown in the upscaled MPI-BGC GPP product, at sites composed primarily of DBF and MF in the northeast, midwest, and southern US shown in (US-Ha1, US-UMB, and US-Dk3 sites in Fig. 2b–d, respectively). Similar results are obtained at other US DBF and MF sites in the northeast and midwest US (see SI) such as US-Syv, US-PFa, US-WCr, and US-MMS (stations in Wisconsin and Indiana) and New England sites (US-Bar and US-Ho1,2). The GOME-2  $F_{740}$  and MPI-BGC GPP seasonal variations also closely follow those from the tower-based GPP estimates at these relatively homogeneous sites.

For most forested sites, GOME-2  $F_{740}$  appears to begin to decline slightly earlier than both GPP estimates. This decline, starting near summer solstice, is consistent with seasonal changes in leaf photosynthetic capacity ( $V_{cmax}$ ) across a variety of tree species reported by Bauerle et al. (2012). It should be noted that the uncertainties in the tower GPP, particularly due to partitioning, are relatively large at this

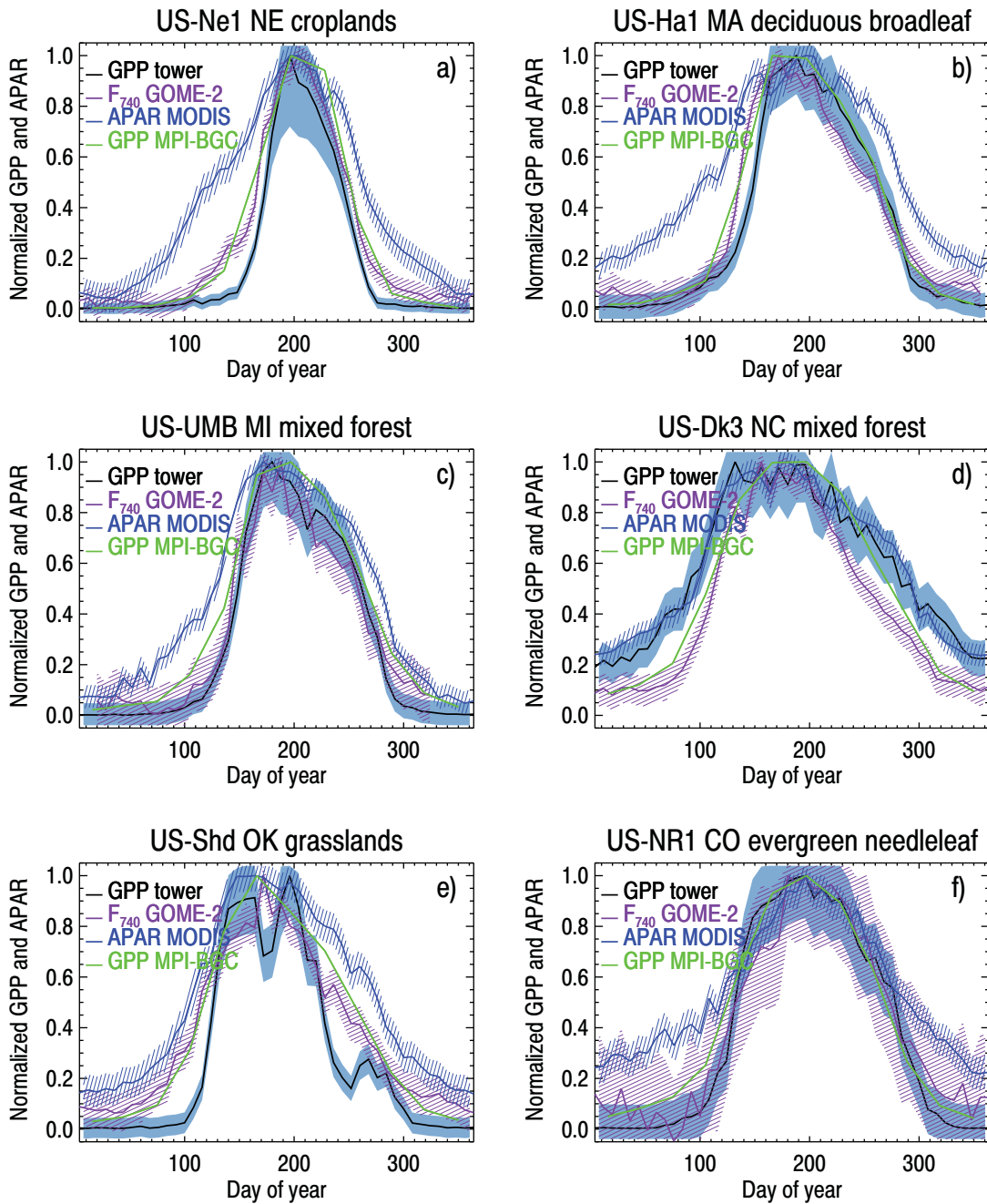


**Fig. 2.** Seasonal cycle (means) of tower-based and upscaled GPP from MPI-BGC, GOME-2  $F_{740}$ , and MODIS-based APAR for a variety of vegetation types. Curves are normalized with respect to unity at the maximum annual value. Contours indicate estimated uncertainties as discussed in the text. Site names, US state, and majority vegetation type within the satellite averaging area are indicated.

time of year. Another explanation is that the seasonal variations in fluorescence efficiency differ slightly from those of light use efficiency.

The Oklahoma US-Shd site shown in Fig. 2e is relatively heterogeneous in terms of vegetation type in the surrounding satellite averaging area and is composed primarily of grasslands. The upscaled GPP from MPI-BGC shows a somewhat more broad and smooth seasonal cycle as compared with the tower-estimated GPP. GOME-2  $F_{740}$  agrees to within estimated uncertainties with the MPI-BGC GPP at this site, while the MODIS APAR shows a more lengthy duration of activity.

GOME-2  $F_{740}$  and MPI-BGC upscaled GPP compare reasonably well with each other as well as with tower GPP at the evergreen needleleaf forest (ENF) US-NR1 site (Fig. 2f). MODIS-based APAR does not show a drop to near zero in winter. This is likely a result of the evergreen vegetation or other non-photosynthetic components that are absorbing

PAR in winter but not engaging in photosynthesis. The GOME-2  $F_{740}$  errors are proportionally higher for this site as compared with the others owing to the overall lower observed values. Therefore, the empirically-derived constant component of the error ( $0.2 \text{ mW/m}^2/\text{nm/sr}$ ) produces an effectively lower signal-to-noise ratio for sites with lower fluorescence signals. Other examples are shown in the Supplemental material for shrublands and savannas that also display low fluorescence values.

The seasonality of GPP and GOME-2  $F_{740}$  at the savanna tower sites in Africa and Australia (see Fig. 3a and c) shows similar patterns. In both cases MODIS-based APAR does not display as much variability as GOME-2  $F_{740}$  or the GPP estimates. In contrast, the evergreen broadleaf forest site in Australia (Fig. 3b) shows different seasonality of both upscaled MPI-BGC GPP and GOME-2  $F_{740}$  as compared with MODIS-

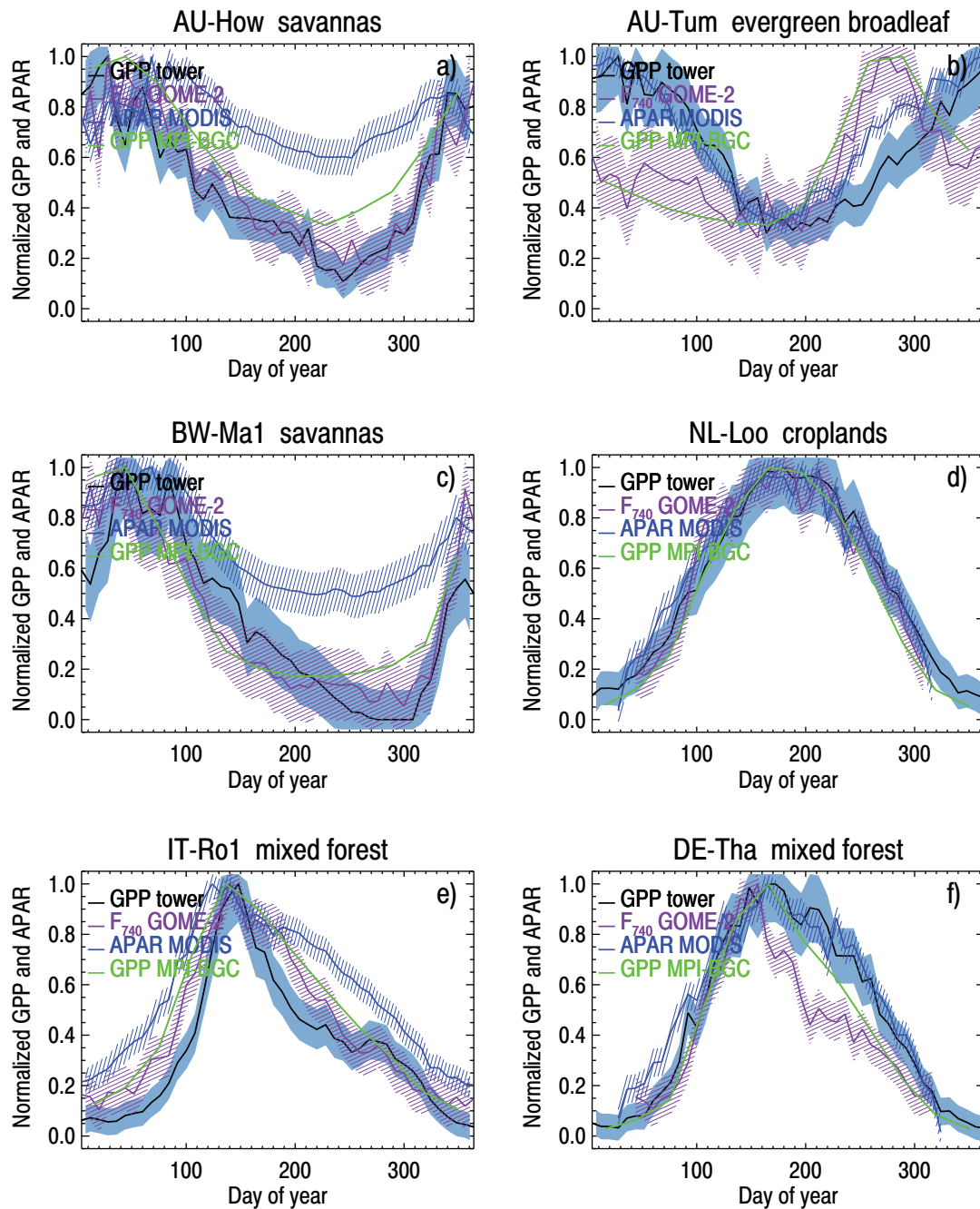


Fig. 3. Similar to Fig. 2 but showing sites from Australia, Africa, and Europe for a variety of vegetation types.

based APAR and tower GPP. This is likely due to spatial heterogeneity around the site that is surrounded by pastures that display a peak in GPP around day 280 similar to that shown in MPI-BGC GPP and GOME-2  $F_{740}$  (J. Beringer, private communication, 2014).

GOME-2  $F_{740}$  tracks the seasonality of GPP reasonably well for the European sites dominated by croplands and mixed-forest within the satellite averaging area (Fig. 3d–f). It should be noted that these sites are also relatively heterogeneous as indicated by differences shown in sites contained within approximately the same satellite averaging area (see SI). In these cases, GOME-2  $F_{740}$  is in good agreement with the upscaled MPI-BGC GPP estimates. However, as shown for the mixed-forest dominated US sites and discussed above, a somewhat earlier decline at the start of senescence is shown for GOME-2  $F_{740}$  as compared with the GPP estimates for the DE-Tha site (Fig. 3f).

In order to show that the displayed seasonal variability of GPP is not driven primarily by the seasonality of PAR, we alternatively repeated this comparison by normalizing GPP estimates and GOME-2  $F_{740}$  with respect to incoming potential PAR (results not shown). This analysis showed that the seasonality of GPP (and GOME-2  $F_{740}$ ) is dictated largely by that of LUE and fPAR. Results in Cheng et al. (2014) support this conclusion.

The general conclusions discussed above were not substantially impacted by varying the value of the  $f_e$  threshold for the GOME-2  $F_{740}$  data. We also checked whether the conclusions hold if tower data are filtered for clouds using the reported incident short-wave radiation. While cloud filtering quantitatively affects monthly-mean GPP and to some extent GOME-2  $F_{740}$  values (changes absolute values), it does not substantially alter the qualitative spatio-temporal variations of normalized GPP.

3.2. Comparisons with multi-model mean weekly GPP

In this section, we examine whether GOME-2  $F_{740}$  offers a means to constrain or validate global vegetation models in terms of the simulated seasonality of photosynthesis. Fig. 4 shows the multi-model weekly mean GPP from data driven (DD) and prognostic (Prog) models along with the tower-based GPP and GOME-2  $F_{740}$  for the same sites as in Fig. 2. The multi-model means, particularly for the DD models, show a somewhat lengthier duration of photosynthesis for northern and midwestern DBF and MF sites such as US-Ha1 and US-UMB, the agricultural US-Ne1 site, and the grasslands US-Shd site as compared with tower-based GPP. Like the MODIS APAR estimates, the models, especially DD models, show better agreement of the estimated GPP seasonal cycle with the tower data for the southern MF-dominated US-Dk3 site.

The models also generally fall within the range of observational uncertainties for the ENF-dominated US-NR1 site.

Some of the DD models contained in the multi-model means calculate GPP using the LUE model as in Eq. (1). Errors in these types of models can result from errors in fPAR and/or LUE. In areas containing dormant green vegetation, such as MF and ENF in winter, APAR may remain high owing to the greenness of the vegetation (including non-chlorophyll containing pigments) when solar radiation is being absorbed but not used for photosynthesis. In this situation, models that utilize reflectance-based parameters like fPAR must then depend upon their LUE parameterization to control GPP.

In regions with cold winters, low winter temperatures are generally sufficient to reduce LUE and subsequently GPP; when LUE can be estimated reliably as near or equal to zero (e.g., temperatures near or

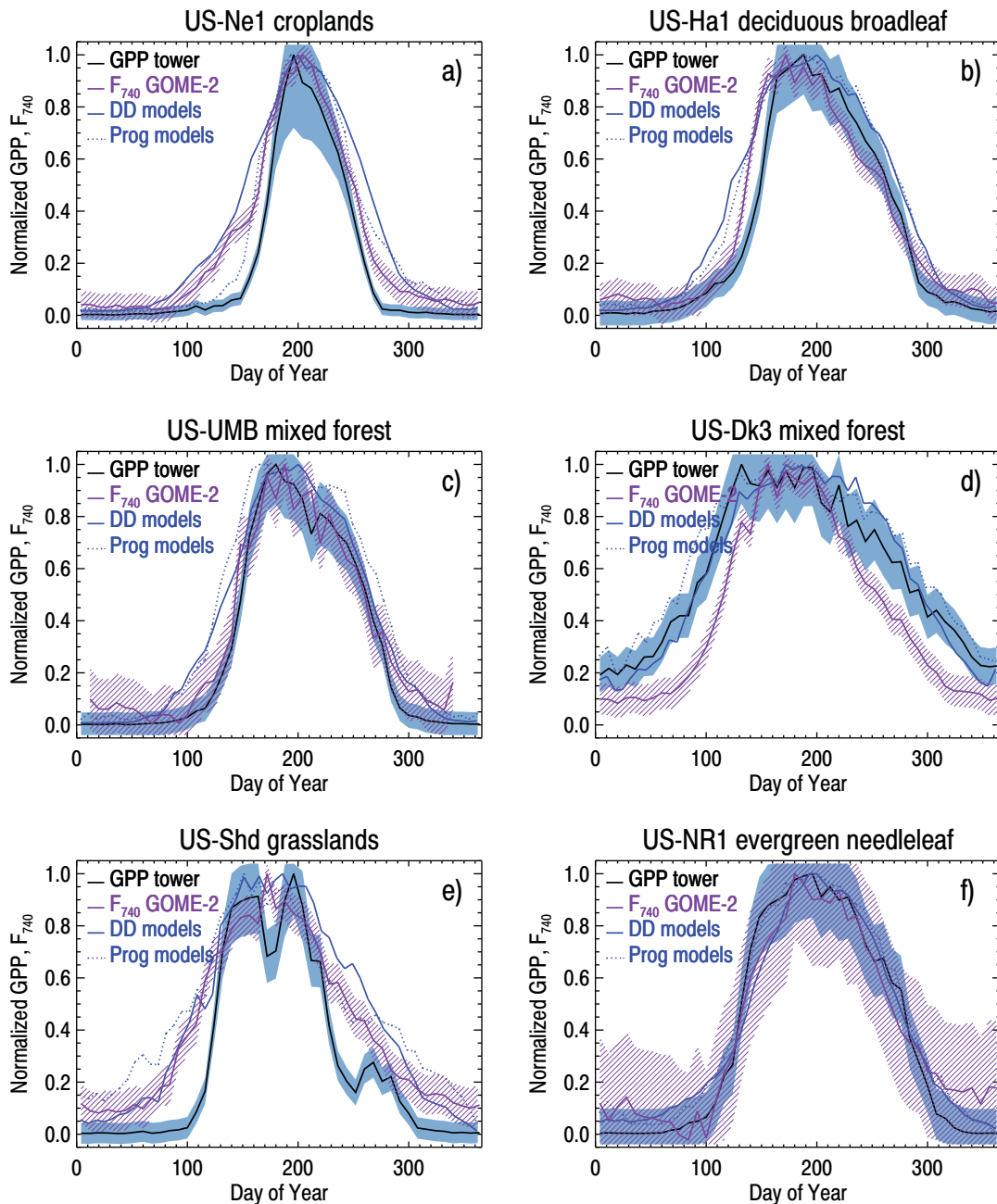


Fig. 4. Similar to Fig. 2 showing seasonal variability in tower-based GPP, GOME-2  $F_{740}$ , and multi-model ensemble means that use data-driven (DD) and prognostic (Prog) approaches to estimate LAI/GPP.

below freezing), it can be assumed that GPP is likewise near or equal to zero. Under these conditions, the GPP estimate is not influenced by any errors in fPAR/APAR.

However, in areas where temperatures are near or above freezing outside of the main part of growing season and fPAR remains high, it is more challenging to estimate the spring initiation and autumn decline of photosynthesis through the LUE parameterization. As a result, an incorrect GPP may be generated outside the main growing season when fPAR is at a moderate value. This has been reported previously for the MODIS GPP product (MOD17) (Heinsch et al., 2006; Turner, Ritts et al., 2003; Turner et al., 2006); MOD17 is one of the models contained in our data-driven ensemble and one that specifically uses the MOD15 fPAR product. Improved seasonal cycles of GPP have been obtained in an LUE model by using fPAR<sub>chl</sub> as compared with MODIS fPAR (fPAR<sub>canopy</sub>) (Cheng et al., 2014).

Our results suggest that GOME-2  $F_{740}$  may provide an additional constraint for estimating the seasonal rise and fall of GPP, particularly for the deciduous and mixed forest sites. Given the results shown in the previous subsection, it is suggested that  $F_{740}$  can offer estimates of the seasonality of photosynthesis in areas not well covered by flux tower measurements that can be used for model validation. In addition, GOME-2  $F_{740}$  provides a global data set at a spatial resolution similar to that of global models.

### 3.3. Timing indicators associated with different stages of photosynthetic activity

There is no standard way to compute phenological indicators, such as onset of greenness or photosynthetic activity in spring, using satellite data (Fisher, Mustard, & Vadeboncoeur, 2006; Gu et al., 2003). It has been shown for deciduous vegetation and many crops that the spring pattern of leaf emergence, followed by rapid growth, and then a stable period of maximum leaf area can be represented using a logistical model (e.g., Zhang et al., 2003, and references therein). A reverse pattern can be modeled for the transition from senescence to dormancy.

We identify various timing indicators following the approach of Zhang et al. (2003) as illustrated in Fig. 5 for the US-Bar site. We have augmented the approach by computing uncertainties for the indicators as described below. The first step is to fit either the greenup or senescence portions of the seasonal cycle of the various parameters (GPP, MODIS APAR, or GOME-2  $F_{740}$ ) to a function of the form

$$y(t) = \frac{c}{1 + e^{a+bt}} + d. \quad (6)$$

Then, using the fitted parameters in Eq. (6), the rate of change in the curvature can be computed analytically. Transition dates are defined for the times when the rate of change in the curvature reaches local minima or maxima.

In the greenup (or declining) portion of the seasonal cycle, the photosynthetic (or senescence) onset is defined as the first peak/valley in the curvature-change rate. The next large peak is known as the inflection or stability point where GPP or satellite parameters are changing at a large rate. The last peak occurs at the onset of maximum photosynthetic activity in the greenup portion or at the onset of dormancy in the declining phase.

Here, we focus exclusively on forested and cropland sites in North America for which this fitting approach works well. We inspected the results for each site and discarded a few sites (e.g., US-Bkg, US-MOZ, US-SP1-3) where the fitting procedure was not well behaved (e.g., owing to a too narrowly peaked maximum, multiple peaks, or incomplete dormancy).

To compute the uncertainties in the timing indicators, we use a Monte Carlo approach centered about the initial fit with 1000 perturbations. To illustrate the range of uncertainties for the rate of change in

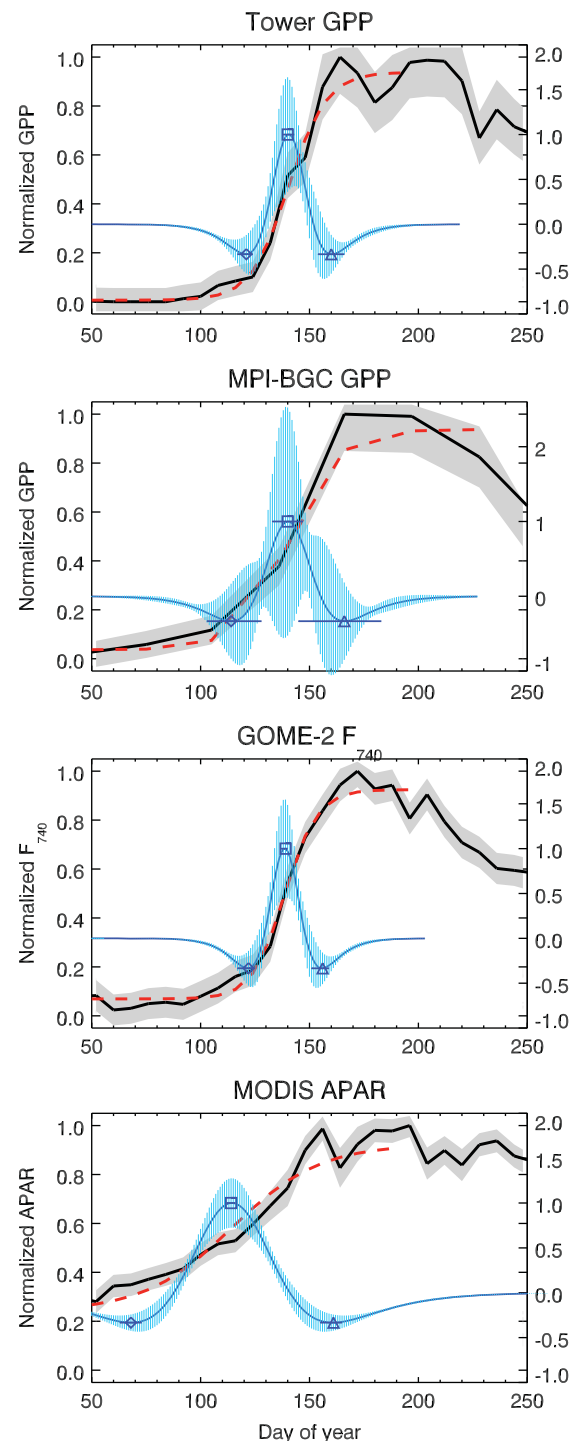


**Fig. 5.** Example of how timing indicators are computed at US-Bar tower; black solid line with gray shading: Normalized curves corresponding to left axes with associated uncertainties; blue solid with vertical bar shading: computed rate of change in the curvature from the fitting logistical function with computed error standard deviations along with timing indicators (symbols) and corresponding uncertainties ( $1\sigma$ , horizontal line) from the Monte Carlo simulation corresponding to right-side axes. (For interpretation of the references to color in this figure legend, the reader is referred to the web version of this article.)

curvature shown in Fig. 5, we use standard linear error analysis to propagate observation errors through the fitting procedure. Specifically, we compute the Jacobian of Eq. (6),  $K$ , and assume that the observation error covariance matrix,  $S_y$  is a diagonal matrix (i.e., errors are assumed

to be unbiased and uncorrelated with respect to each other). The estimated error covariance for the fitted parameters in Eq. (6),  $S_f$ , is given by

$$S_f = \left( K^t (S_y)^{-1} K \right)^{-1} \quad (7)$$

$S_f$  is then further propagated linearly using Eq. (7) with the analytically computed Jacobian of the rate of change of curvature function (see Zhang et al., 2003, for formulation of the rate of change of curvature). This provides a full error covariance for the rate of change of curvature. We show the error standard deviations for reference in Fig. 5 (note that errors are correlated with respect to each other). The errors from the Monte Carlo simulation for the timing parameters are also shown in Fig. 5.

The computed timing indicators and associated uncertainties are shown in Figs. 6–7 for tower and upscaled GPP, GOME-2  $F_{740}$ , MODIS APAR, and the multi-model mean (results from both DD and Prog models are averaged together here). Note that the indicators for the multi-model means are available only for Ameriflux sites. Bias and  $\chi^2$  statistics with respect to the tower GPP (considered as the standard) are computed and averaged for each vegetation type and summarized in Table 2. Again, note that the multi-model mean uses only the available Ameriflux sites to compute these statistics.

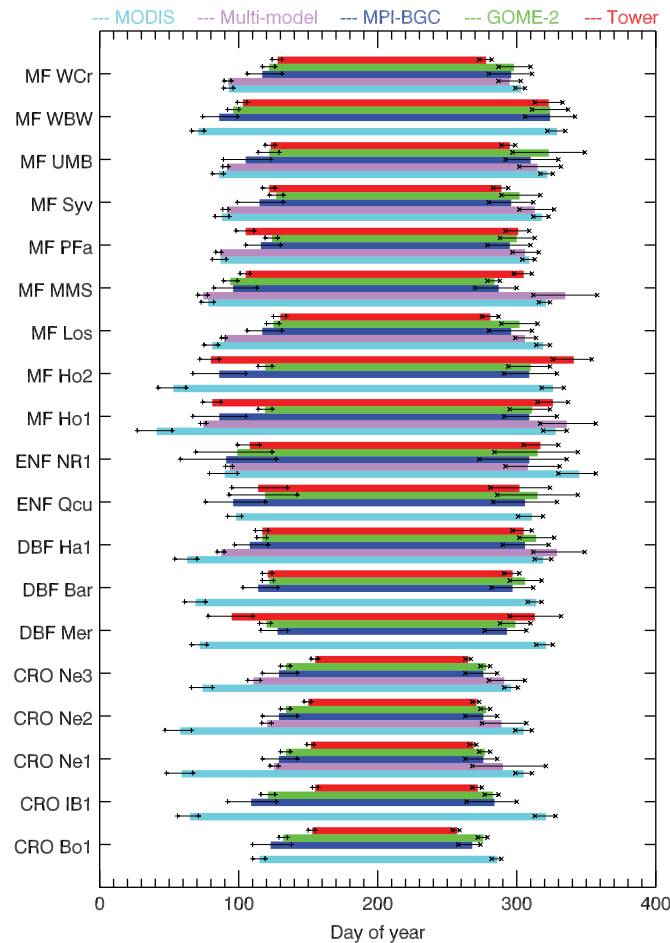


**Fig. 6.** Summary of the duration of photosynthesis from the photosynthetic onset (left end of horizontal bars with uncertainties indicated) to the dormancy onset (right end of horizontal bars) (see text for details) for various forest and cropland sites and data sets. The site name and majority IGBP vegetation type are indicated on the left. Timing indicators derived from the multi-model mean data are only available for Ameriflux sites. (For interpretation of the references to color in this figure, the reader is referred to the web version of this article.)

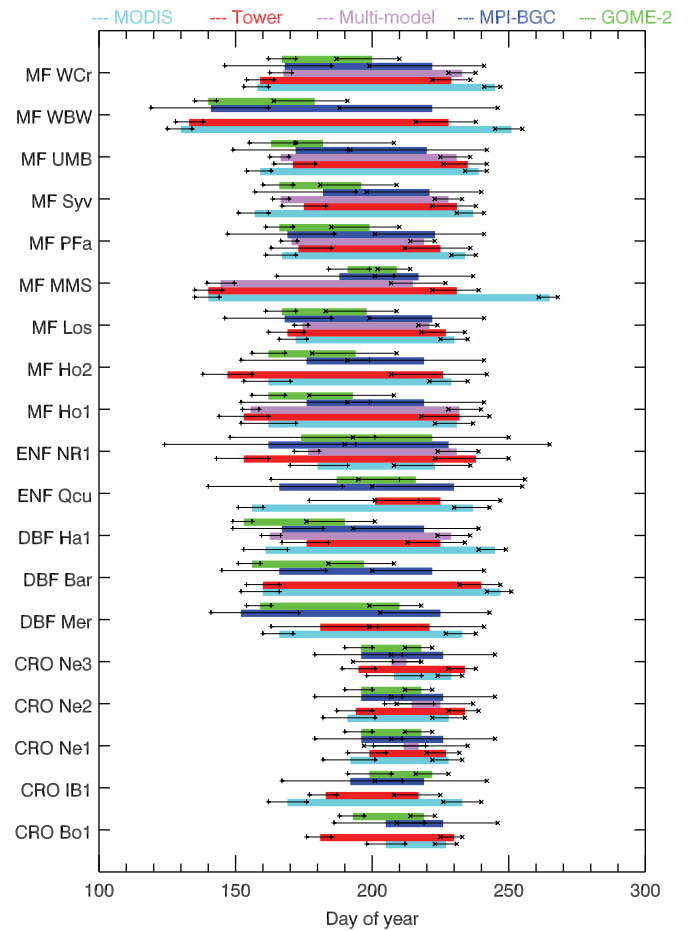


**Fig. 7.** Similar to Fig. 6 but showing the duration of maximum photosynthesis from onset of maximum photosynthesis (left end of horizontal bars) to the senescence onset (right end of horizontal bars).

Fig. 6 shows the duration of photosynthesis (similar to the carbon uptake period), from the onset of photosynthesis (the left edge of the various colored bars with corresponding uncertainties) to the onset of dormancy on the right edge of the bars. For MF and DBF sites in the northeast and northern midwest US, the photosynthesis onset according to the tower-based data occurs between about days 70 and 130. For these sites, both the MPI-BGC GPP and GOME-2  $F_{740}$  track the tower onset reasonably well, while MODIS-based APAR shows a substantially earlier rise ranging from ~days 60–90. The multi-model mean shows a similar early onset of photosynthesis for many of these sites. Photosynthetic onset from MODIS APAR compares better with the tower data for the ENF-dominated sites.

For the midwest cropland sites, the onset of photosynthesis occurs much later, generally around day 150 according to the tower estimates. The larger scale GOME-2  $F_{740}$  and MPI-BGC GPP detects photosynthetic onset somewhat earlier, around days 110–135, likely due to a mixture of other vegetation types within their averaging area. Despite the fact that the MODIS data are averaged over a much smaller area near the tower site, the MODIS APAR results again show a substantially earlier photosynthesis onset between days 50 and 80 for all agricultural sites except US-Bo1 where the onset was near day 115. The multi-model mean onset of photosynthesis is generally comparable to the MPI-BGC GPP results for the US-NE1–3 cropland sites.

Similarly, for the onset of dormancy in Fig. 6 (the end of the colored bars), MODIS APAR is somewhat late with respect to the tower data for croplands. The MPI-BGC GPP and GOME-2  $F_{740}$  dormancy onset estimates are closer to the tower data and also closer to each other for croplands. For most of the MF and DBF sites, GOME-2  $F_{740}$  provides

**Table 2**

Statistics for various timing indicators versus the standard (tower GPP). Significant differences in terms of the  $\chi^2$  statistic ( $>2.0$ ) are shown in bold. The units of bias are days.

| Type   | Onset       |       | Onset       |      | Inflection  |       | Inflection  |       | Onset max. |       | Onset      |       |
|--|-------------|-------|-------------|------|-------------|-------|-------------|-------|------------|-------|------------|-------|
|  | Photosyn.   |       | Dormancy    |      | Spring      |       | Autumn      |       | Photosyn.  |       | Senesce.   |       |
|  | $\chi^2$    | Bias  | $\chi^2$    | Bias | $\chi^2$    | Bias  | $\chi^2$    | Bias  | $\chi^2$   | Bias  | $\chi^2$   | Bias  |
| <i>MODIS APAR vs. tower GPP</i>                  |             |       |             |      |             |       |             |       |            |       |            |       |
| CRO  | <b>71.9</b> | −78.8 | <b>30.3</b> | 35.8 | <b>60.9</b> | −38.0 | <b>16.7</b> | 18.6  | <b>2.3</b> | 2.6   | 0.6        | 0.6   |
| DBF  | <b>21.0</b> | −43.0 | 2.0         | 13.0 | <b>22.0</b> | −26.3 | <b>5.1</b>  | 12.7  | 0.7        | −10.0 | 1.0        | 13.0  |
| ENF  | 1.1         | −17.0 | 1.1         | 18.5 | 1.4         | −13.0 | 0.3         | 8.0   | <b>3.3</b> | −9.0  | 0.4        | −1.5  |
| MF   | <b>21.2</b> | −33.2 | <b>7.5</b>  | 15.1 | <b>20.1</b> | −17.1 | <b>11.5</b> | 12.9  | 0.8        | −1.4  | <b>2.2</b> | 10.8  |
| <i>MPI BGC GPP vs. tower GPP</i>                 |             |       |             |      |             |       |             |       |            |       |            |       |
| CRO  | <b>3.9</b>  | −29.2 | 0.5         | 9.2  | 1.1         | −11.0 | 0.1         | 2.6   | 0.3        | 6.6   | 0.1        | −3.8  |
| DBF  | 0.9         | 5.7   | 0.2         | −6.3 | 0.2         | −2.3  | 0.3         | −6.7  | 0.4        | −10.7 | 0.2        | −6.7  |
| ENF  | 0.3         | −17.5 | 0.0         | −2.0 | 0.7         | −15.0 | 0.1         | −3.0  | 0.5        | −13.0 | 0.0        | −2.5  |
| MF   | 0.5         | −5.9  | 0.7         | −1.9 | 0.6         | 3.9   | 0.4         | −5.3  | 0.6        | 13.3  | 0.1        | −8.8  |
| <i>GOME-2 <math>F_{740}</math> vs. tower GPP</i> |             |       |             |      |             |       |             |       |            |       |            |       |
| CRO  | <b>19.6</b> | −22.0 | <b>5.9</b>  | 11.6 | <b>3.2</b>  | −8.0  | 0.9         | 1.0   | 1.0        | 5.6   | <b>2.1</b> | −9.4  |
| DBF  | 0.5         | 8.7   | 0.4         | 1.3  | 1.4         | −3.7  | <b>3.7</b>  | −14.3 | 1.5        | −16.3 | <b>3.9</b> | −29.7 |
| ENF  | 0.0         | −2.0  | 0.1         | 5.5  | 0.1         | 0.5   | 0.3         | 11.0  | 0.3        | 3.5   | 0.1        | −12.5 |
| MF   | <b>2.6</b>  | 7.9   | 1.6         | 1.7  | <b>5.3</b>  | 7.7   | <b>5.7</b>  | −16.4 | <b>2.4</b> | 7.1   | <b>3.5</b> | −34.9 |
| <i>Multi-model mean vs. tower GPP</i>            |             |       |             |      |             |       |             |       |            |       |            |       |
| CRO  | <b>47.3</b> | −33.5 | 1.5         | 21.7 | 0.6         | −6.2  | 0.2         | 3.0   | <b>3.0</b> | 16.8  | 1.2        | −15.3 |
| DBF  | <b>11.9</b> | −29.5 | 1.2         | 23.9 | <b>14.5</b> | −20.5 | 1.0         | 13.9  | 1.1        | −13.5 | 0.1        | 3.9   |
| ENF  | 1.2         | −14.5 | 0.1         | −9.0 | 0.5         | 4.5   | 0.4         | −8.0  | <b>2.2</b> | 23.5  | 0.2        | −7.0  |
| MF   | <b>19.9</b> | −27.6 | <b>2.1</b>  | 18.6 | <b>9.7</b>  | −13.3 | 1.5         | 7.2   | 0.4        | 0.8   | 0.3        | −4.5  |

dormancy onset estimates that are generally within uncertainty ranges of both MPI-BGC and tower-based GPP. The MODIS APAR and multi-model mean dormancy onset results are somewhat late with respect to the tower data for several sites but still fall within the uncertainty ranges for other sites. The dormancy onset results for the ENF sites from all estimates agree relatively well with each other to within the uncertainties.

Fig. 7 shows the duration of maximum photosynthesis from the onset of maximum photosynthesis and senescence onset; uncertainties tend to be larger for these estimates. The onset of maximum photosynthesis derived from the various datasets is in general agreement to within the relatively large uncertainties.

In contrast with the onset of dormancy, GOME-2  $F_{740}$  shows consistently early onset of senescence for MF and DBF sites, although the error bars are quite large for some sites. This was similarly shown in Section 3.1 in the seasonal plots for representative sites. Again, this could be an indication that  $\theta_F$  starts to decline slightly earlier than LUE, although errors bars for GOME-2  $F_{740}$  and MPI-BGC generally overlap. Additional ground-based fluorescence and other measurements would be helpful to sort out this issue.

Table 2 highlights the cases of statistically significant differences in the timing indicators with respect to the tower GPP (considered to be the standard) and reinforces conclusions drawn from the barplots. For example, MODIS-based APAR and the multi-model mean show an early onset of photosynthesis for croplands, DBF, and MF in general as compared with the tower estimates. This early onset is also reflected in the multi-model mean for the same IGBP types. The early rise in MODIS APAR continues to the spring inflection point for these biomes which is not the case for the multi-model mean.

GOME-2  $F_{740}$  and MPI-BGC GPP show an early onset of photosynthesis for croplands; this could be related to their larger spatial footprints. GOME-2  $F_{740}$  has a significant early bias in the onset of senescence for croplands, DBF, and MF sites even with the relatively large error bars. MODIS APAR also shows later dates for dormancy onset and the autumn inflection point for some vegetation types. GOME-2  $F_{740}$  shows a late bias in dormancy onset in croplands that again could be related to the spatial footprint. MPI-BGC GPP similarly shows a late bias, but it is not statistically significant given the estimated errors. Both MPI-BGC GPP

and GOME-2  $F_{740}$  show early biases in the autumn inflection point for DBF and MF sites, though the biases are significant only for GOME-2  $F_{740}$ .

Tables 3–5 summarize the results of the timing indicators for representative cropland and forested sites. The results are divided by majority biome type within the satellite averaging area and are ordered

**Table 3**

Summary of duration of photosynthesis, growing season (length between inflection points), and duration of maximum photosynthesis as described in the text with uncertainties in parentheses for majority agricultural sites.

| Estimate                       | Duration of photosyn. | Duration of growing season | Duration of max. photosyn. |
|--------------------------------|-----------------------|----------------------------|----------------------------|
| <i>US-Bo1 40.01°N –88.29°E</i> |                       |                            |                            |
| MODIS                          | 171 (4.0)             | 97 (2.1)                   | 22 (5.7)                   |
| Tower                          | 104 (2.5)             | 76 (2.3)                   | 49 (4.3)                   |
| MPI-BGC                        | 145 (11.4)            | 83 (10.9)                  | 21 (17.5)                  |
| GOME-2                         | 144 (3.3)             | 85 (1.8)                   | 26 (4.5)                   |
| <i>US-Ne1 41.17°N –96.48°E</i> |                       |                            |                            |
| MODIS                          | 246 (7.9)             | 142 (3.0)                  | 36 (7.8)                   |
| Tower                          | 117 (2.5)             | 73 (3.5)                   | 28 (6.5)                   |
| MPI-BGC                        | 147 (12.0)            | 88 (9.0)                   | 30 (17.6)                  |
| GOME-2                         | 143 (3.8)             | 82 (2.0)                   | 22 (5.0)                   |
| Multi-model                    | 165 (18.9)            | 85 (9.7)                   | 6 (15.0)                   |
| <i>US-Ne2 41.16°N –96.47°E</i> |                       |                            |                            |
| MODIS                          | 247 (7.9)             | 142 (3.0)                  | 37 (7.9)                   |
| Tower                          | 121 (2.5)             | 80 (3.0)                   | 40 (6.0)                   |
| MPI-BGC                        | 147 (12.0)            | 88 (9.0)                   | 30 (17.6)                  |
| GOME-2                         | 144 (3.5)             | 83 (2.0)                   | 22 (5.0)                   |
| Multi-model                    | 169 (11.6)            | 90 (5.8)                   | 11 (11.8)                  |
| <i>US-Ne3 41.18°N –96.44°E</i> |                       |                            |                            |
| MODIS                          | 222 (6.4)             | 122 (3.2)                  | 21 (7.8)                   |
| Tower                          | 110 (2.3)             | 75 (2.3)                   | 39 (5.5)                   |
| MPI-BGC                        | 147 (12.0)            | 88 (9.0)                   | 30 (17.6)                  |
| GOME-2                         | 144 (3.5)             | 83 (2.0)                   | 22 (5.0)                   |
| Multi-model                    | 181 (9.7)             | 82 (7.2)                   | 6 (9.5)                    |
| <i>US-IB1 41.86°N –88.22°E</i> |                       |                            |                            |
| MODIS                          | 256 (7.5)             | 160 (3.0)                  | 64 (7.0)                   |
| Tower                          | 117 (2.9)             | 76 (4.0)                   | 34 (7.0)                   |
| MPI-BGC                        | 175 (17.8)            | 101 (13.8)                 | 27 (21.3)                  |
| GOME-2                         | 162 (5.0)             | 92 (2.5)                   | 23 (7.1)                   |

**Table 4**

Similar to Table 3 but for deciduous broadleaf forest (DBF) and evergreen needleleaf forest (ENF) sites as indicated.

| Estimate                               | Duration of photosyn. | Duration of growing season | Duration of max. photosyn. |
|--|-----------------------|----------------------------|----------------------------|
| <i>US-Ha1 (DBF) 42.54°N – 72.17°E</i>  |                       |                            |                            |
| MODIS                                  | 256 (7.1)             | 170 (3.0)                  | 84 (6.7)                   |
| Tower                                  | 188 (5.9)             | 119 (3.8)                  | 49 (9.6)                   |
| MPI-BGC                                | 198 (14.4)            | 125 (10.3)                 | 52 (20.0)                  |
| GOME-2                                 | 197 (9.2)             | 117 (3.7)                  | 37 (9.2)                   |
| Multi-model                            | 241 (13.2)            | 153 (8.2)                  | 66 (4.9)                   |
| <i>US-Bar (DBF) 44.06°N – 71.29°E</i>  |                       |                            |                            |
| MODIS                                  | 245 (6.4)             | 166 (2.9)                  | 87 (5.9)                   |
| Tower                                  | 176 (4.6)             | 129 (2.8)                  | 80 (6.8)                   |
| MPI-BGC                                | 183 (13.8)            | 120 (8.1)                  | 56 (19.8)                  |
| GOME-2                                 | 184 (8.6)             | 113 (3.4)                  | 41 (8.9)                   |
| <i>CA-Mer (DBF) 45.41°N – 75.52°E</i>  |                       |                            |                            |
| MODIS                                  | 249 (5.8)             | 158 (2.5)                  | 67 (5.5)                   |
| Tower                                  | 218 (17.3)            | 129 (9.8)                  | 40 (20.3)                  |
| MPI-BGC                                | 165 (12.6)            | 119 (6.9)                  | 73 (18.1)                  |
| GOME-2                                 | 179 (8.3)             | 115 (3.2)                  | 51 (7.4)                   |
| <i>US-NR1 (ENF) 40.03°N – 105.55°E</i> |                       |                            |                            |
| MODIS                                  | 255 (11.9)            | 149 (5.9)                  | 43 (12.4)                  |
| Tower                                  | 209 (10.5)            | 148 (4.5)                  | 85 (11.7)                  |
| MPI-BGC                                | 218 (33.0)            | 141 (29.6)                 | 66 (36.3)                  |
| GOME-2                                 | 216 (28.8)            | 132 (19.8)                 | 48 (27.5)                  |
| Multi-model                            | 215 (13.9)            | 136 (7.2)                  | 55 (6.2)                   |
| <i>CA-Qcu (ENF) 49.27°N – 74.04°E</i>  |                       |                            |                            |
| MODIS                                  | 213 (7.3)             | 147 (3.5)                  | 81 (5.6)                   |
| Tower                                  | 188 (20.8)            | 106 (16.3)                 | 24 (21.6)                  |
| MPI-BGC                                | 210 (22.3)            | 137 (14.9)                 | 64 (26.0)                  |
| GOME-2                                 | 196 (26.8)            | 143 (23.2)                 | 29 (27.2)                  |

by latitude. These tables highlight that there is significantly more variability in the timing indicators for the ENF and MF sites that cover a larger range of latitudes. For example, the southern-most MF site (US-WBW) has a significantly longer duration of photosynthesis than most of the more northern sites as determined from tower and upscaled GPP as well as GOME-2  $F_{740}$ . Some of the MF sites at similar latitudes also show significant differences; the northern midwestern sites, US-UMB and US-WCr (as well as other sites located nearby and not shown in the table), have significantly shorter durations of photosynthesis as compared with the US-Ho1 site located in the northeast US at a similar latitude, and US-UMB has a longer duration of photosynthesis as compared with US-WCr. Again, this is shown by tower and upscaled GPP as well as GOME-2  $F_{740}$ . While MODIS and multi-model mean data produce significantly larger estimates of duration of photosynthesis, they generally show the same spatial variability.

We attempted to compare individual yearly estimates of the timing parameters from GOME-2  $F_{740}$ , MPI-BGC GPP, and available flux tower measurements. In general, the interannual variability is smaller than the estimated uncertainties. To reduce uncertainties in the current data sets, we would need to average data over larger (regional) scales. We intend to pursue this in more detail in future studies.

**4. Conclusions and ongoing work**

Our direct comparisons of GOME-2  $F_{740}$  with tower-based and upscaled GPP indicate that GOME-2  $F_{740}$  tracks the spring onset and autumn decline of photosynthesis for several different biomes. Moderate to high values of MODIS-derived fPAR (>0.2–0.5) are maintained throughout the year at many sites for which green vegetation may absorb light but not utilize the energy for photosynthesis, particularly in winter. Our study suggests that GOME-2  $F_{740}$  may be used to better constrain this aspect of GPP simulated by data-driven models and improve parameterizations in process-based models. We acknowledge the inherent difficulties in comparing the relatively small spatial scale tower-based GPP estimates with those of the

**Table 5**

Similar to Table 3 but for representative mixed forest sites.

| Estimate                        | Duration of photosyn. | Duration of growing season | Duration of max. photosyn. |
|---------------------------------|-----------------------|----------------------------|----------------------------|
| <i>US-WBW 35.96°N – 84.29°E</i> |                       |                            |                            |
| MODIS                           | 258 (5.6)             | 189 (2.3)                  | 121 (4.8)                  |
| Tower                           | 220 (7.5)             | 158 (3.2)                  | 95 (8.5)                   |
| MPI-BGC                         | 238 (15.5)            | 159 (11.3)                 | 81 (25.5)                  |
| GOME-2                          | 228 (9.6)             | 134 (3.7)                  | 39 (10.0)                  |
| <i>US-MMS 39.32°N – 86.41°E</i> |                       |                            |                            |
| MODIS                           | 243 (4.3)             | 184 (1.8)                  | 125 (4.0)                  |
| Tower                           | 200 (5.2)             | 145 (3.0)                  | 91 (7.0)                   |
| MPI-BGC                         | 191 (15.3)            | 110 (12.3)                 | 29 (19.8)                  |
| GOME-2                          | 190 (4.8)             | 103 (2.5)                  | 18 (6.8)                   |
| Multi-model                     | 260 (16.5)            | 165 (10.7)                 | 70 (7.9)                   |
| <i>US-Ho1 45.20°N – 68.74°E</i> |                       |                            |                            |
| MODIS                           | 287 (10.7)            | 177 (4.1)                  | 69 (8.6)                   |
| Tower                           | 245 (9.0)             | 162 (4.3)                  | 79 (10.9)                  |
| MPI-BGC                         | 223 (19.0)            | 133 (13.8)                 | 43 (24.3)                  |
| GOME-2                          | 192 (10.8)            | 111 (5.9)                  | 31 (11.8)                  |
| Multi-model                     | 261 (14.2)            | 168 (9.6)                  | 76 (4.7)                   |
| <i>US-UMB 45.56°N – 84.71°E</i> |                       |                            |                            |
| MODIS                           | 236 (4.3)             | 157 (2.0)                  | 80 (4.3)                   |
| Tower                           | 172 (4.3)             | 118 (3.3)                  | 64 (7.8)                   |
| MPI-BGC                         | 205 (18.0)            | 127 (12.3)                 | 48 (23.1)                  |
| GOME-2                          | 201 (19.1)            | 112 (14.4)                 | 19 (14.1)                  |
| Multi-model                     | 223 (10.7)            | 144 (5.1)                  | 64 (4.6)                   |
| <i>US-WCr 45.81°N – 90.08°E</i> |                       |                            |                            |
| MODIS                           | 210 (3.5)             | 149 (1.8)                  | 87 (3.8)                   |
| Tower                           | 150 (4.0)             | 111 (2.5)                  | 70 (6.1)                   |
| MPI-BGC                         | 179 (14.1)            | 116 (8.3)                  | 54 (20.3)                  |
| GOME-2                          | 176 (8.7)             | 105 (3.8)                  | 33 (8.9)                   |
| Multi-model                     | 202 (5.9)             | 134 (2.4)                  | 65 (4.5)                   |

larger-footprint GOME-2 data that were produced for different sets of years. The use of the MPI-BGC upscaled GPP estimates for the same time periods as the GOME-2 data has provided a means of assessing potential differences arising from the differing spatial scales and temporal periods of tower- and satellite-based data.

Ecosystem models and reflectance-based data products from Earth-orbiting satellites (e.g., NDVI, EVI, LAI) are currently used to predict or monitor the seasonal dynamics of vegetated ecosystems that correspond with the growing season and carbon uptake period. However, as noted above, these models and satellite observations often do a poor job of describing the length of the growing season, as found in our current study and by others (e.g., Garrity et al., 2011; Richardson et al., 2012). Over- and under-estimation of the growing season and related carbon uptake period can lead to errors in predicting interannual variability in ecosystem-atmosphere carbon exchange and can negatively impact our ability to assess long term trends in ecosystem response to climate change (Garrity et al., 2011). Reflectance-based satellite products are typically linked to seasonal morphological development of plant canopies (e.g., LAI). Time lags between morphological and physiological development can lead to significant error in estimating seasonal carbon flux (Morecroft, Stokes, & Morison, 2003; Richardson et al., 2009, 2010). In contrast, our results show very good agreement between GPP and fluorescence for several important vegetation types (croplands and several forest types); this suggests that GOME-2  $F_{740}$  may better capture seasonal dynamics of canopy physiology relevant to carbon flux in some ecosystems as compared with existing models and satellite data products.

Following the recent launch of a second GOME-2 instrument on the MetOp-B platform, the MetOp-A GOME-2 is now operating in a smaller pixel mode (since day 196 of 2013); ground pixels are now 40 × 40 km<sup>2</sup> with a 960 km wide swath. The MetOp-B operates in the standard wider swath mode as described above. This enables smaller pixel fluorescence observations of similar quality although with less frequent overpasses. Use of the two GOME-2 instruments should lead to improved

fluorescence data sets for further studies in the future. In addition, the upcoming launches of the Orbiting Carbon Observatory-2 (OCO-2) (Frankenberg, Butz, & Toon, 2011; Frankenberg et al., 2014) and the Sentinel-5 precursor TROPOMI (Veefkind et al., 2012) will enable additional measurements near the O<sub>2</sub>-A band at higher spatial resolution. The Fluorescence EXplorer (FLEX) (Rascher, 2007), an ESA Explorer 8 Mission selected for Phase A/B1 in early 2011, is designed specifically to make chlorophyll fluorescence measurements (Guanter et al., 2010) and would provide additional spectral information across the visible-NIR spectrum.

### Acknowledgment

Funding for this work was provided in part by the NASA Carbon Cycle Science program (NNH10DA001N). The authors gratefully acknowledge EUMETSAT and the MODIS data processing team for making available the GOME-2 and MODIS data sets, respectively, used here as well as the algorithm development teams. We also thank James Collatz, Randy Kawa, William Cook, Yen-Ben Cheng, Larry Corp, Petya Campbell, Qingyuan Zhang, and Arlindo da Silva for helpful discussions. We are indebted to Philip Durbin for assistance with the GOME-2 satellite data set. We also thank Joshua Fisher and an anonymous reviewer for helpful comments that helped to improve the paper.

This study uses eddy covariance data acquired by the FLUXNET community and in particular by the following networks: AmeriFlux (U.S. Department of Energy, Biological and Environmental Research, Terrestrial Carbon Program (DEFG0204ER63917 and DEFG0204ER63911)) AfriFlux, CarboAfrica, CarboEuropeIP, CarboItaly, CarboMont, FluxnetCanada (supported by the CFCAS, NSERC, BIOCAP, Environment Canada, and NRCAN), GreenGrass, KoFlux, LBA, NECC, OzFlux, and USCCC. We acknowledge the financial support to the eddy covariance data harmonization provided by the CarboEuropeIP, FAO/TOSTCO, iLEAPS, Max Planck Institute for Biogeochemistry, National Science Foundation, University of Tuscia, Wageningen University CALM Group (Climate change and Adaptive Land and Water Management), Universit Laval and Environment Canada and U.S. Department of Energy and the database development and technical support from the Berkeley Water Center, Lawrence Berkeley National Laboratory, Microsoft Research eScience, Oak Ridge National Laboratory, University of California Berkeley, University of Virginia, and South Dakota State University. Sites in the U.S. also acknowledge support from the National Science Foundation (NSF), U.S. Department of Agriculture (USDA), and the U.S. Department of Energy (DOE). Funding for this research was also provided by the Biological and Environmental Research Program (BER), U.S. DOE, through the Midwestern Center of the National Institute for Global Environmental Change (NIGEC) under Cooperative Agreements DE-FC03-90ER61010, and from the BER under Cooperative Agreements DE-FG02-03ER63624 and DE-FG03-01ER63278, NOAA grant NA09OAR4310063, and NASA grants NNX10AR63G and NNX11A008A. Any opinions, findings, and conclusions or recommendations expressed in this publication are those of the authors and do not necessarily reflect the views of the DOE. Access to the MMSF AmeriFlux site is provided by the Indiana Department of Natural Resources, Division of Forestry. The ZA-Kru site was supported by the NASA Terrestrial Ecology Program (Grant # NNX08A177G) and NSF Biocomplexity Program (Grant # EAR-0120630) through grants to NPH. The OzFlux sites (AU-Wac, AU-Fog, AU-How) were provided by Jason Beringer who was funded under an Australian Research Council FT (FT1110602) and project support from DP130101566. Support for collection and archiving was provided through the Australia Terrestrial Ecosystem Research Network (TERN) (<http://www.tern.org.au>).

The authors are indebted to the all of the PIs and collaborators of the flux tower sites used here who enabled this study including Jason Beringer (AU-Fog, AU-How, AU-Wac), Eva Vangorsel (AU-Tum), Almut Arneth (BW-Ma1), Nigel Roulet, Peter Lafleur, Elyn Humphries, Angela Kross (CA-Mer), Hank Margolis (CA-Qcu), Christian Bernhofer,

Thomas Grünwald (DE-Tha), Dan Yakir (IL-Yat), Dario Pappalardo (IT-Amp, IT-Cpz, IT-Ro1), Jan Elbers, Eddy Moors, Wilma Jans (NL-Loo), Ko J. van Huissteden, Luca Beletti Marchesini (NL-Hor), Margaret Torn, Dave Billesbach (US-ARM), Allen Goldstein (US-Blo), Ram Oren, Gabriel Katul, Paul Stoy, Kim Novick (US-Dk3), J. William Munger (US-Ha1), David Hollinger (US-Ho1–US-Ho2), Roser Matamala, David Cook, Miquel Gonzalez-Meler (US-IB1–US-IB2), Ankur Desai, Ken Davis, and Paul Bolstad (US-Los, US-PFa, US-Syv, US-WCr), Beverly Law (US-Me2–US-Me5), Danilo Dragoni (US-MMS), Lianhong Gu (US-MOZ), Shashi Verma, Andrew Suyker, Joseph Berry, Todd Schimelfenig (US-Ne1–US-Ne3, US-Shd), Russell K. Monson (US-NR1), Dennis Baldocchi (US-Ton, US-Var), Jiquan Chen (US-Oho), Walter Oechel (US-SO2), Timothy Martin (US-SP1–US-SP3), Peter Curtis, Gil Bohrer (US-UMB), Andrew Richardson (US-Bar), and Tilden Meyers (US-Aud, US-Bkg, US-Bo1, US-FPe, US-Goo, US-WBW), Niall P. Hanan, Robert J. Scholes (ZA-Kru).

### Appendix A. Supplementary data

Supplementary data to this article can be found online at <http://dx.doi.org/10.1016/j.rse.2014.06.022>.

### References

- Amoros-Lopez, J., Gomez-Chova, L., Vila-Frances, J., Alonso, L., Calpe, J., Moreno, J., et al. (2008). Evaluation of remote sensing of vegetation fluorescence by the analysis of diurnal cycles. *International Journal of Remote Sensing*, 29, 5423–5436.
- Baldocchi, D.D., Black, T. A., Curtis, P. A., Falge, E., Fuentes, J.D., Granier, A., et al. (2004). Predicting the onset of net carbon uptake by deciduous forests with soil temperature and climate data: A synthesis of FLUXNET data. *International Journal of Biometeorology*, 49, 377–387.
- Baldocchi, D.D., Falge, E., Gu, L. H., Olson, R., Hollinger, D., Running, S., et al. (2001). FLUXNET: A new tool to study the temporal and spatial variability of ecosystem-scale carbon dioxide, water vapor, and energy flux densities. *Bulletin of the American Meteorological Society*, 82, 2415–2434.
- Barr, A. G., Ricciuto, D.M., Schaefer, K., Richardson, A.D., Agarwal, D., Thornton, P. E., et al. (2013). NACP site: Tower meteorology, flux observations with uncertainty, and ancillary data, data set. Oak Ridge, Tennessee, USA: Oak Ridge National Laboratory Distributed Active Archive Center (<http://dxdoi.org/103334/ORNLDAA/1178>).
- Barr, A. G., Richardson, A.D., Hollinger, D. Y., Papale, D., Arain, M.A., Black, T. A., et al. (2013). Use of change-point detection for friction-threshold evaluation in eddy-covariance studies. *Agricultural and Forest Meteorology*, 171–172, 31–45.
- Bauerle, W. L., Oren, R., Way, D. A., Qian, S. S., Stoy, P. C., Thornton, P. E., et al. (2012). Photoperiodic regulation of the seasonal pattern of photosynthetic capacity and the implications for carbon cycling. *Proceedings of the National Academy of Sciences*. <http://dx.doi.org/10.1073/pnas.1119131109>.
- Beringer, J., Hacker, J., Hutley, L. B., Leuning, R., Arndt, S. K., Amiri, R., et al. (2011). SPECIAL – Savanna patterns of energy and carbon integrated across the landscape. *Bulletin of the American Meteorological Society*, 92, 1467–1485.
- Beringer, J., Livesley, S. J., Randle, J., & Hutley, L. B. (2013). Carbon dioxide fluxes dominate the greenhouse gas exchanges of a seasonal wetland in the wet-dry tropics of northern Australia. *Agricultural and Forest Meteorology*, 182–183, 239–247.
- Berry, J., Frankenberg, C., Wennberg, P., Baker, I., Bowman, K., Castro-Contreras, S., et al. (2013). New methods for measurements of photosynthesis from space. Presented at the 2013 NASA Terrestrial Ecology Science Team Meeting, La Jolla, CA, April 30–May 2, 2013 (<http://www.kiss.caltech.edu/workshops/photosynthesis2012/NewMethod2.pdf>).
- Billesbach, D. P., Fischer, M. L., Torn, M. S., & Berry, J. A. (2004). A portable eddy covariance system for the measurement of ecosystem–atmosphere exchange of CO<sub>2</sub>, water vapor, and energy. *Journal of Atmospheric and Oceanic Technology*, 21, 639–650.
- Bonan, G. B., Lawrence, P. J., Oleson, K. W., Levis, S., Jung, M., Reichstein, M., et al. (2011). Improving canopy processes in the Community Land Model version 4 (CLM4) using global flux fields empirically inferred from FLUXNET data. *Journal of Geophysical Research*, G02014. <http://dx.doi.org/10.1029/2010JG001593>.
- Bracho, R. G., Starr, G., Gholz, H. L., Martin, T. A., Cropper, W. P., Jr., & Loescher, H. W. (2012). Controls on carbon dynamics by ecosystem structure and climate for southeastern U.S. slash pine plantations. *Ecological Monographs*, 82, 101–128.
- Campbell, P. K. E., Middleton, E. M., Corp, L. A., & Kim, M. S. (2008). Contribution of chlorophyll fluorescence to the apparent vegetation reflectance. *Science of the Total Environment*, 404, 433–439.
- Chappelle, E. W., & Williams, D. L. (1987). Laser-induced fluorescence (LIF) from plant foliage. *IEEE Transactions on Geoscience and Remote Sensing*, GE-25, 726–736.
- Cheng, Y. B., Zhang, Z., Lyapustin, A. I., Wang, Y., & Middleton, E. M. (2014). Impacts of light use efficiency and fPAR parameterization on carbon modeling. *Agricultural and Forest Meteorology*, 189–190, 187–197.
- Churkina, G., Schimel, D., Braswell, B. H., & Xiao, X. (2005). Spatial analysis of growing season length control over net ecosystem exchange. *Global Change Biology*, 11, 1777–1787. <http://dx.doi.org/10.1111/j.1365-2486.2005.001012.x>.

- Cook, B.D., Davis, K.J., Wang, W., Desai, A.R., Berger, B.W., Teclaw, R.M., et al. (2004). Carbon exchange and venting anomalies in an upland deciduous forest in northern Wisconsin, USA. *Agricultural and Forest Meteorology*, 126, 271–295. <http://dx.doi.org/10.1016/j.agrformet.2004.06.008>.
- Corp, L. A., McMurtrey, J. E., Middleton, E. M., Mulchi, C. L., Chappelle, E. W., & Daughtry, C. S. T. (2003). Fluorescence sensing systems: In vivo detection of biophysical variations in field corn due to nitrogen supply. *Remote Sensing of the Environment*, 86, 470–4793.
- Davis, K. J., Bakwin, P.S., Berger, B. W., Yi, C., Zhao, C., Teclaw, R. M., et al. (2003). The annual cycle of CO<sub>2</sub> and H<sub>2</sub>O exchange over a northern mixed forest as observed from a very tall tower. *Global Change Biology*, 9, 1278–1293.
- Desai, A.R., Bolstad, P. V., Cook, B.D., Davis, K. J., & Carey, E. V. (2005). Comparing net ecosystem exchange of carbon dioxide between an old-growth and mature forest in the upper Midwest, USA. *Agricultural and Forest Meteorology*, 128, 33–55.
- Desai, A.R., Richardson, A.D., Moffat, A.M., Kattge, J., Hollinger, D. Y., Barr, A., et al. (2008). Cross-site evaluation of eddy covariance GPP and RE decomposition techniques. *Agricultural and Forest Meteorology*, 148, 821–838.
- Dragonì, D., Schmid, H. P., Grimmond, C. S. B., & Loescher, H. W. (2007). Uncertainty of annual net ecosystem productivity estimated using eddy covariance flux measurements. *Journal of Geophysical Research*, 112, D17102. <http://dx.doi.org/10.1029/2006JD008149>.
- Dragonì, D., Schmid, H. P., Wayson, C. A., Potter, H., Grimmond, C. S. B., & Randolph, J. C. (2010). Evidence of increased net ecosystem productivity associated with a longer vegetated season in a deciduous forest in south-central Indiana, USA. *Global Change Biology*, 17, D17102. <http://dx.doi.org/10.1111/j.1365-2486.2010.02281.x> (886–897).
- Elbers, J. A., Jacobs, C. M. J., Kruijt, B., Jans, W. W. P., & Moors, Eddy J. (2011). Assessing the uncertainty of estimated annual totals of net ecosystem productivity: A practical approach applied to a mid latitude temperate pine forest. *Agricultural and Forest Meteorology*, 151, 1823–1830. <http://dx.doi.org/10.1016/j.agrformet.2011.07.020> (ISSN 0168-1923).
- Fisher, J. I., Mustard, J. F., & Vadeboncoeur, M.A. (2006). Green leaf phenology at Landsat resolution: Scaling from the field to the satellite. *Remote Sensing of Environment*, 100, 265–279.
- Flexas, J., Escalona, J. M., Evain, S., Guliás, S. J., Moya, I., Osmond, C. B., et al. (2002). Steady-state chlorophyll fluorescence (Fs) measurements as a tool to follow variations of net CO<sub>2</sub> assimilation and stomatal conductance during water-stress in C<sub>3</sub> plants. *Physiologia Plantarum*, 114, 231–240.
- Frankenberg, C., Butz, A., & Toon, G. C. (2011). Disentangling chlorophyll fluorescence from atmospheric scattering effects in O<sub>2</sub>A-band spectra of reflected sun-light. *Geophysical Research Letters*, 38, L03801. <http://dx.doi.org/10.1029/2010GL045896>.
- Frankenberg, C., Fisher, J. B., Worden, J., Badgley, G., Saatchi, S. S., Lee, J. E., et al. (2011). New global observations of the terrestrial carbon cycle from GOSAT: Patterns of plant fluorescence with gross primary productivity. *Geophysical Research Letters*, 38, L17706. <http://dx.doi.org/10.1029/2011GL048738>.
- Frankenberg, C., O'Dell, C., Berry, J., Guanter, L., Joiner, J., Köhler, P., et al. (2014). Prospects for chlorophyll fluorescence remote sensing from the orbiting carbon observatory-2. *Remote Sensing of Environment*, 147, 1–12.
- Frankenberg, C., O'Dell, C., Guanter, L., & McDuffie, J. (2012). Remote sensing of near-infrared chlorophyll fluorescence from space in scattering atmospheres: Implications for its retrieval and interferences with atmospheric CO<sub>2</sub> retrievals. *Atmospheric Measurement Techniques*, 5, 2081–2094.
- Garbulsky, M. F., Penuelas, J., Papale, D., & Filella, I. (2008). Remote estimation of carbon dioxide uptake by a Mediterranean forest. *Global Change Biology*, 14, 2860–2867.
- Garrity, S. R., Bohrer, G., Maurer, K. D., Mueller, K. L., Vogel, C. S., & Curtis, P.S. (2011). A comparison of multiple phenology data sources for estimating seasonal transitions in deciduous forest carbon exchange. *Agricultural and Forest Meteorology*, 151, 1741–1752.
- Giasson, M. -A., Coursolle, C., & Margolis, H. A. (2006). Ecosystem-level carbon fluxes from a boreal cutover in eastern Canada before and after scarification. *Agricultural and Forest Meteorology*, 140, 23–40. <http://dx.doi.org/10.1016/j.agrformet.2006.08.001>.
- Gilmanov, T. G., Aires, L., Barcza, Z., Baron, V. S., Belelli, L., Beringer, J., et al. (2010). Productivity, respiration, and light-response parameters of world grassland and agroecosystems derived from flux-tower measurements. *Rangeland Ecology Management*, 63, 16–39.
- Gilmanov, T. G., Tieszen, L. L., Wylie, B. K., Flanagan, L. B., Frank, A. B., Haferkamp, M. R., et al. (2005). Integration of CO<sub>2</sub> flux and remotely-sensed data for primary production and ecosystem respiration analyses in the Northern Great Plains: Potential for quantitative spatial extrapolation. *Global Ecology and Biogeography*, 14, 271–292. <http://dx.doi.org/10.1111/j.1466-822X.2005.00151.x>.
- Gilmanov, T. G., Verma, S. B., Sims, P. L., Meyers, T. P., Bradford, J. A., Burba, G. G., et al. (2003). Gross primary production and light response parameters of four Southern Plains ecosystems estimated using long-term CO<sub>2</sub>-flux tower measurements. *Global Biogeochemical Cycles*, 17, 1071. <http://dx.doi.org/10.1029/2002GB002023>.
- Goldstein, A. H., Hultman, N. E., Fracheboud, J. M., Bauer, M. R., Panek, J. A., Xu, M., et al. (2000). Effects of climate variability on the carbon dioxide, water, and sensible heat fluxes above a ponderosa pine plantation in the Sierra Nevada (CA). *Agricultural and Forest Meteorology*, 101, 113–129.
- Gough, C. M., Hardiman, B., Vogel, C. S., Nave, L., & Curtis, P.S. (2010). Wood net primary production resilience in an unmanaged forest transitioning from early to middle succession. *Forest Ecology and Management*, 260, 36–41.
- Goulden, M. L., Munger, J. W., Fan, S. M., Daube, B. C., & Wofsy, S.C. (1996). Measurements of carbon sequestration by long-term eddy covariance: Methods and a critical evaluation of accuracy. *Global Change Biology*, 2, 169–182.
- Grünwald, T., & Bernhofer, C. (2007). A decade of carbon, water and energy flux measurements of an old spruce forest at the Ancher Station Tharandt. *Tellus*, 59B, 387–396.
- Gu, L., Hanson, P. J., Mac Post, W., Kaiser, D. P., Yang, B., Nemani, R., et al. (2008). The 2007 eastern US spring freezes: Increased cold damage in a warming world? *Bioscience*, 58, 253–262.
- Gu, L., Massman, W. J., Leuning, R., Pallardy, S. G., Meyers, T., Hanson, P. J., et al. (2012). The fundamental equation of eddy covariance and its application in flux measurements. *Agricultural and Forest Meteorology*, 152, 135–148.
- Gu, L., Meyers, T., Pallardy, S. G., Hanson, P. J., Yang, B., Heuer, M., et al. (2006). Direct and indirect effects of atmospheric conditions and soil moisture on surface energy partitioning revealed by a prolonged drought at a temperate forest site. *Journal of Geophysical Research*, D16102. <http://dx.doi.org/10.1029/2006JD007161>.
- Gu, L., Post, W. M., Baldocchi, D.D., Black, T. A., Suyker, A. E., Verma, S. B., et al. (2009). Characterizing the seasonal dynamics of plant community photosynthesis across a range of vegetation types. *Phenology of ecosystem processes*. Dordrecht/New York: Springer.
- Gu, L., Post, W. M., Baldocchi, D.D., Black, T. A., Verma, S. B., Vesala, T., et al. (2003). Phenology of vegetation photosynthesis. In M.D. Schwartz (Ed.), *Phenology: An integrated environmental science* (pp. 467–485). Dordrecht: Kluwer.
- Guanter, L., Alonso, L., Gómez-Chova, L., Amorós-López, Vila-Francés, J., & Moreno, J. (2007). Estimation of solar-induced vegetation fluorescence from space measurements. *Geophysical Research Letters*, 34. <http://dx.doi.org/10.1029/2007GL029289>.
- Guanter, L., Alonso, L., Gómez-Chova, L., Meroni, M., Preusker, R., Fischer, J., et al. (2010). Developments for vegetation fluorescence retrieval from spaceborne high-resolution spectrometry in the O<sub>2</sub>-A and O<sub>2</sub>-B absorption bands. *Journal of Geophysical Research*, 115, D19303. <http://dx.doi.org/10.1029/2009JD013716>.
- Guanter, L., Frankenberg, C., Dudhia, A., Lewis, P. E., Gómez-Dans, J., Kuze, A., et al. (2012). Retrieval and global assessment of terrestrial chlorophyll fluorescence from GOSAT space measurements. *Remote Sensing of Environment*, 121, 236–251.
- Guanter, L., Rossini, M., Colombo, R., Meroni, M., Frankenberg, C., Lee, J. -E., et al. (2013). Using field spectroscopy to assess the potential of statistical approaches for the retrieval of sun-induced chlorophyll fluorescence from space. *Remote Sensing of Environment*, 133, 52–61.
- Guanter, L., Zhang, Y., Yung, M., Joiner, J., Voigt, M., Berry, J. A., et al. (2014). Global and time-resolved monitoring of crop photosynthesis with chlorophyll fluorescence. *Proceedings of the National Academy of Science*. <http://dx.doi.org/10.1073/pnas.1320008111>.
- Heinsch, F., Zhao, M., Running, S., Kimball, J., Nemani, R., Davis, K., et al. (2006). Evaluation of remote sensing based terrestrial productivity from MODIS using regional tower eddy flux network observations. *IEEE Transactions on Geoscience and Remote Sensing*, 44, 1908–1925.
- Hendriks, D.M.D., Dolman, A. J., Van der Molen, M. K., & Van Huissteden, J. (2008). A compact and stable eddy covariance set-up for methane measurements using off-axis integrated cavity output spectroscopy. *Atmospheric Chemistry and Physics*, 8, 431–443.
- Hendriks, D.M.D., van Huissteden, J., Dolman, A. J., & van der Molen, M. K. (2007). The full greenhouse gas balance of an abandoned peat meadow. *Biogeosciences*, 4, 411–424.
- Huntzinger, D. N., Post, W. M., Wei, Y., Michalak, A.M., West, T. O., Jacobson, A.R., et al. (2012). North American Carbon Program (NACP) regional interim synthesis: Terrestrial biospheric model intercomparison. *Ecological Modelling*, 232, 144–157.
- Jenkins, J. P., Richardson, A.D., Braswell, B. H., Ollinger, S. V., Hollinger, D. Y., & Smith, M. -L. (2007). Refining light-use efficiency calculations for a deciduous forest canopy using simultaneous tower-based carbon flux and radiometric measurements. *Agricultural and Forest Meteorology*, 143, 64–79.
- Joiner, J., Guanter, L., Lindstrot, R., Voigt, M., Vasilkov, A. P., Middleton, E. M., et al. (2013). Global monitoring of terrestrial chlorophyll fluorescence from moderate spectral resolution near-infrared satellite measurements: Methodology, simulations, and application to GOME-2. *Atmospheric Measurement Techniques*, 6, 2803–2823. <http://dx.doi.org/10.5194/amt-6-2803-2013>.
- Joiner, J., Yoshida, Y., Vasilkov, A. P., Yoshida, Y., Corp, L. A., & Middleton, E. M. (2011). First observations of global and seasonal terrestrial chlorophyll fluorescence from space. *Biogeosciences*, 8, 637–651. <http://dx.doi.org/10.5194/bg-8-637-2011>.
- Joiner, J., Yoshida, Y., Vasilkov, A. P., Yoshida, Y., Middleton, E. M., Campbell, P. K. E., et al. (2012). Filling-in of broad far-red solar lines by terrestrial fluorescence and atmospheric Raman scattering as detected by GOME-2 satellite measurements. *Atmospheric Measurement Techniques*, 4, 6185–6228. <http://dx.doi.org/10.5194/amt-4-6185-2011>.
- Jung, M., Reichstein, M., & Bondeau, A. (2009). Towards global empirical upscaling of FLUXNET eddy covariance observations: Validation of a model tree ensemble approach using a biosphere model. *Biogeosciences*, 6, 2001–2013.
- Jung, M., Reichstein, M., Margolis, H. A., Cescatti, A., Richardson, A.D., Arain, M.A., et al. (2011). Global patterns of land-atmosphere fluxes of carbon dioxide, latent heat, and sensible heat derived from eddy covariance, satellite, and meteorological observations. *Journal of Geophysical Research*, 116. <http://dx.doi.org/10.1029/2010JG001566>.
- Kilinc, M., Beringer, J., Hutley, L. B., Tapper, N. J., & McGuire, D. A. (2013). Carbon and water exchange of the world's tallest angiosperm forest. *Agricultural and Forest Meteorology*, 182–183, 215–224.
- Kross, A. (2011). *Characterization of the variability and controls of the carbon dioxide exchange in northern peatlands*. (PhD thesis). McGill University.
- Lafleur, P.M., Roulet, N. T., & Admiral, S. W. (2001). Annual cycle of CO<sub>2</sub> exchange at a bog peatland. *Journal of Geophysical Research*, 106, 3071–3081.
- Loescher, H. W., Law, B. E., Mahrt, L., Hollinger, D. Y., Campbell, J., & Wofsy, S.C. (2006). Uncertainties in, and interpretation of, carbon flux estimates using the eddy covariance technique. *Journal of Geophysical Research*, 111, D21S90.
- Louis, J., Ounis, A., Ducruet, J. -M., Evain, S., Laurila, T., Thum, T., et al. (2005). Remote sensing of sunlight-induced chlorophyll fluorescence and reflectance of Scots pine in the boreal forest during spring recovery. *Remote Sensing of the Environment*, 96, 37–48.

- Luo, Y., Medlyn, B., Hui, D., Ellsworth, D., Reynolds, J., & Katul, G. (2001). Gross primary productivity in Duke Forest: Modeling synthesis of CO<sub>2</sub> experiment and eddy-flux data. *Ecological Applications*, *11*, 239–252.
- Ma, X., Huete, A., Yu, Q., Restrepo, C. N., Davies, K., Broich, M., et al. (2013). Spatial patterns and temporal dynamics in savanna vegetation phenology across the North Australian Tropical Transect. *Remote Sensing of Environment*, *139*, 97–115.
- Meroni, M., Picchi, V., Rossini, M., Cogliati, S., Panigada, C., Nali, C., et al. (2008). Leaf level early assessment of ozone injuries by passive fluorescence and photochemical reflectance index. *International Journal of Remote Sensing*, *29*, 5409–5422.
- Meroni, M., Rossini, M., Guanter, L., Alonso, L., Rascher, U., Colombo, R., et al. (2009). Remote sensing of solar-induced chlorophyll fluorescence: Review of methods and applications. *Remote Sensing of Environment*, *113*, 2037–2051.
- Middleton, E. M., Cheng, Y., Corp, L. A., Huemmerich, K. F., Kustas, W., & Campbell, P. K. E. (2010). Diurnal and directional responses of chlorophyll fluorescence and the PRI in a cornfield. *4th International Workshop on Remote Sensing of Vegetation Fluorescence, Valencia, Spain, November 15–17, 2010* (6 pp.).
- Middleton, E. M., Corp, L. A., & Campbell, P. K. E. (2008). Comparison of measurements and FluorMOD simulations for solar induced chlorophyll fluorescence and reflectance of a corn crop under nitrogen treatments. *International Journal of Remote Sensing*, *29*, 5193–5213.
- Migliavacca, M., Reichstein, M., Richardson, A.D., Colombo, R., Sutton, M.A., Lasslop, G., et al. (2010). Semiempirical modeling of abiotic and biotic factors controlling ecosystem respiration across eddy covariance sites. *Global Change Biology*, *17*, 390–409. <http://dx.doi.org/10.1111/j.1365-2486.2010.02243.x>.
- Misson, L., Baldocchi, D., Black, T., Blanken, P., Brunet, Y., Curieluste, J., et al. (2007). Partitioning forest carbon fluxes with overstory and understory eddy-covariance measurements: A synthesis based on FLUXNET data. *Agricultural and Forest Meteorology*, *144*, 14–31.
- Monson, R. K., Turnipseed, A. A., Sparks, J. P., Harley, P. C., Scott-Denton, L. E., Sparks, K., et al. (2002). Carbon sequestration in a high-elevation, subalpine forest. *Global Change Biology*, *8*, 459–478.
- Monteith, J. L. (1972). Solar radiation and productivity in tropical ecosystems. *Journal of Applied Ecology*, *9*, 747–766.
- Morecroft, M.D., Stokes, V. J., & Morison, J. I. L. (2003). Seasonal changes in the photosynthetic capacity of canopy oak (*Quercus robur*) leaves: The impact of slow development on annual carbon uptake. *International Journal of Biometeorology*, *47*, 221–226.
- Moya, I., Camenen, L., Evain, S., Goulas, Y., Cerovic, Z. G., Latouche, G., et al. (2004). A new instrument for passive remote sensing: 1. Measurements of sunlight-induced chlorophyll fluorescence. *Remote Sensing of the Environment*, *91*, 186–197.
- Munro, R., Eisinger, M., Anderson, C., Callies, J., Corpaccioli, E., Lang, R., et al. (2006). GOME-2 on MetOp, from in-orbit verification to routine operations. *Proceedings of EUMETSAT Meteorological Satellite Conference, Helsinki, Finland, 12–16 June 2006*.
- Myeni, R. B., Hoffman, W., Knyazikhin, Y., Privette, J. L., Glassy, J., Tian, Y., et al. (2002). Global products of vegetation leaf area and fraction absorbed PAR from year one of MODIS data. *Remote Sensing of Environment*, *83*, 214–231.
- Oak Ridge National Laboratory Distributed Active Archive Center (ORNL DAAC) (2010). *MODIS subsetted land products, collection 5*. Available on-line [<http://daac.ornl.gov/MODIS/modis.html>] from Oak Ridge, Tennessee, U.S.A.: ORNL DAAC (Accessed Nov. 11, 2011).
- Piao, S., Ciais, P., Friedlingstein, P., Peylin, P., Reichstein, M., Luyssaert, S., et al. (2008). Net carbon dioxide losses of northern ecosystems in response to autumn warming. *Nature*, *451*, 49–53.
- Powell, T. L., Gholz, H. L., Clark, K. L., Starr, G., Cropper, W. P., Jr., & Martin, T. A. (2008). Carbon exchange of a mature naturally-regenerated pine forest in north Florida. *Global Change Biology*, *14*, 2523–2538.
- Randerson, J. T., Field, C. B., Fung, I. Y., & Tans, P. P. (1999). Increases in early season ecosystem uptake explain recent changes in the seasonal cycle of atmospheric CO<sub>2</sub> at high northern latitudes. *Geophysical Research Letters*, *26*, 2765–2768. <http://dx.doi.org/10.1029/1999GL900500>.
- Rascher, U. (2007). FLEX – fluorescence explorer: A remote sensing approach to quantify spatio-temporal variations of photosynthetic efficiency from space. *Photosynthesis Research*, *91*, 293–294.
- Rascher, U., Agati, G., Alonso, L., Cecchi, G., Champagne, S., Colombo, R., et al. (2009). CEFLES2: The remote sensing component to quantify photosynthetic efficiency from the leaf to the region by measuring sun-induced fluorescence in the oxygen absorption bands. *Biogeosciences*, *6*, 1181–1198.
- Richardson, A.D., Anderson, R. S., Arain, M.A., Barr, A. G., Bohrer, G., Chen, G., et al. (2012). Terrestrial biosphere models need better representation of vegetation phenology: Results from the North American Carbon Program Site Synthesis. *Global Change Biology*, *18*, 566–584. <http://dx.doi.org/10.1111/j.1365-2486.2011.02562.x>.
- Richardson, A.D., Black, T. A., Ciais, P., Delbart, N., Friedl, M.A., Gobron, N., et al. (2010). Influence of spring and autumn phenological transitions on forest ecosystem productivity. *Philosophical Transactions of the Royal Society, Series B*, *365*, 3227–3246. <http://dx.doi.org/10.1098/rstb.2010.0102>.
- Richardson, A.D., Hollinger, D. Y., Dail, B., Lee, J. T., Munger, J. W., & OKeefe, J. (2009). Influence of spring phenology on seasonal and annual carbon balance in two contrasting New England forests. *Tree Physiology*, *29*, 321–331. <http://dx.doi.org/10.1093/treephys/tpn040>.
- Rosema, A., Verhoef, W., Schoote, J., & Snel, J. F. H. (1991). Simulating fluorescence light-canopy interaction in support of laser-induced fluorescence measurements. *Remote Sensing of Environment*, *37*, 117–130.
- Rotenberg, E., & Yakir, D. (2010). Contribution of semi-arid forests to the climate system. *Science*, *327*, 451–454. <http://dx.doi.org/10.1126/science.1179998>.
- Running, S. W., Nemani, R. R., Heinsch, F. A., Zhao, M., Reeves, M., & Hashimoto, H. (2004). A continuous satellite-derived measure of global terrestrial primary production. *BioScience*, *54*, 547–560.
- Schaefer, K., Schwalm, C. R., Williams, C., Altaf Arain, M., Barr, A., Chen, J. M., et al. (2012). A model-data comparison of gross primary productivity: Results from the North American Carbon Program site synthesis. *Journal of Geophysical Research*, *117*, G03010. <http://dx.doi.org/10.1029/2012JG001960>.
- Schmid, H. P., Grimmer, C. S. B., Cropley, F., Offerle, B., & Su, H. B. (2000). Measurements of CO<sub>2</sub> and energy fluxes over a mixed hardwood forest in the mid-western United States. *Agricultural and Forest Meteorology*, *103*, 357–374.
- Scholes, R. J., Gureja, N., Giannecchini, M., Dovie, D., Wilson, B., Davidson, N., et al. (2001). The environment and vegetation of the flux measurement site near Skukuza, Kruger National Park. *Koedoe*, *44*, 73–83.
- Sims, D. A., Rahman, A. F., Cordova, V. D., Baldocchi, D.D., Flanagan, L. B., Goldstein, A. H., et al. (2005). Midday values of gross CO<sub>2</sub> flux and light use efficiency during satellite overpasses can be used to directly estimate eight-day mean flux. *Agricultural and Forest Meteorology*, *131*, 1–12.
- Stammes, P., Sneep, M., de Haan, J., Veeffkind, J. P., Wang, P., & Levelt, P. F. (2008). Effective cloud fractions from the Ozone Monitoring Instrument: Theoretical framework and validation. *Journal of Geophysical Research*, *113*, D16S38. <http://dx.doi.org/10.1029/2007JD008820>.
- Stoy, P. C., Katul, G. G., Siqueira, M. B.S., Juang, J. Y., Novick, K. A., McCarthy, H. R., et al. (2008). Role of vegetation in determining carbon sequestration along ecological succession in the southeastern United States. *Global Change Biology*, *14*, 1409–1427.
- Stylinski, C. D., Gamon, J. A., & Oechel, W. C. (2002). Seasonal patterns of reflectance indices, carotenoid pigments and photosynthesis of evergreen chaparral species. *Oecologia*, *131*, 366–374.
- Sulman, B. N., Desai, A.R., Cook, B.D., Saliendra, N., & Mackay, D. S. (2009). Contrasting carbon dioxide fluxes between a drying shrub wetland in Northern Wisconsin, USA, and nearby forests. *Biogeosciences*, *6*, 1115–1126.
- Sun, G., Alstad, K., Chen, J., Chen, S., Ford, C. R., Lin, G., et al. (2010). A general predictive model for estimating monthly ecosystem evapotranspiration. *Ecohydrology*, *4*, 245–255.
- Suyker, A. E., Verma, S. B., Burba, G. G., & Arkebauer, T. J. (2005). Gross primary production and ecosystem respiration of irrigated maize and irrigated soybean during a growing season. *Agricultural and Forest Meteorology*, *131*, 180–190.
- Thornton, P. E., Law, B. E., Gholz, H. L., Clark, K. L., Falge, E., Ellsworth, D. S., et al. (2002). Modeling and measuring the effects of disturbance history and climate on carbon and water budgets in evergreen needleleaf forests. *Agricultural and Forest Meteorology*, *113*, 185–222.
- Turner, D. P., Rifts, W. D., Cohen, W. B., Gower, S. T., Running, S. W., Zhao, M., et al. (2006). Evaluation of MODIS NPP and GPP products across multiple biomes. *Remote Sensing of Environment*, *102*, 282–292.
- Turner, D. P., Ritts, W. D., Cohen, W. B., Gower, S. T., Zhao, M., Running, S. W., et al. (2003). Scaling Gross Primary Production (GPP) over boreal and deciduous forest landscapes in support of MODIS GPP product validation. *Remote Sensing of Environment*, *88*, 256–270.
- Turner, D. P., Urbansky, S., Bremer, D., Wofsy, S.C., Meyers, T., Gower, S. T., et al. (2003). A cross-biome comparison of daily light use efficiency for gross primary production. *Global Change Biology*, *9*, 383–395.
- Urbanski, S., Barford, C., Wofsy, S., Kucharik, C., Pyle, E., Budney, J., et al. (2007). Factors controlling CO<sub>2</sub> exchange on timescales from hourly to decadal at Harvard Forest. *Journal of Geophysical Research*, *112*, #G02020.
- van der Tol, C., Verhoef, W., & Rosema, A. (2009). A model for chlorophyll fluorescence and photosynthesis at leaf scale. *Agricultural and Forest Meteorology*, *149*, 96–105.
- Vasilkov, A., Joiner, J., & Spurr, R. (2013). Note on rotational-Raman scattering in the O<sub>2</sub> A- and B-bands. *Atmospheric Measurement Techniques*, *6*, 981–990. <http://dx.doi.org/10.5194/amt-6-981-2013>.
- Veeffkind, J. P., Aben, I., McMullan, K., Forster, H., de Vries, J., Otter, G., et al. (2012). TROPOMI on the ESA Sentinel-5 Precursor: A GMES mission for global observations of the atmospheric composition for climate, air quality and ozone layer applications. *Remote Sensing of Environment*, *120*, 70–83.
- Veenendaal, E. M., Kolle, O. L. A. F., & Lloyd, J. (2004). Seasonal variation in energy fluxes and carbon dioxide exchange for a broad-leaved semi-arid savanna (Mopane woodland) in Southern Africa. *Global Change Biology*, *10*, 318–328.
- Verma, S. B., Dobermann, A., Cassman, K. G., Walters, D. T., Knops, J. M., Arkebauer, T. J., et al. (2005). Annual carbon dioxide exchange in irrigated and rainfed maize-based agroecosystems. *Agricultural and Forest Meteorology*, *131*, 77–96.
- Wang, Z., Xiao, X., & Yan, X. (2010). Modeling gross primary production of maize cropland and degraded grassland in northeastern China. *Agricultural and Forest Meteorology*, *150*, 1160–1167.
- White, M.A., & Nemani, R. R. (2003). Canopy duration has little influence on annual carbon storage in the deciduous broad leaf forest. *Global Change Biology*, *9*, 967–972.
- Xiao, X., Hollinger, D. Y., Aber, J.D., Goltz, M., Davidson, E. A., Zhang, Q., et al. (2004). Satellite-based modeling of gross primary production in an evergreen needleleaf forest. *Remote Sensing of Environment*, *89*, 519–534.
- Xiao, J. F., Zhuang, Q. L., Baldocchi, D.D., Law, B. E., Richardson, A.D., Chen, J. Q., et al. (2008). Estimation of net ecosystem carbon exchange for the conterminous United States by combining MODIS and AmeriFlux data. *Agricultural and Forest Meteorology*, *148*, 1827–1847.
- Yuan, W., Liu, S., Zhou, G., Zhou, G., Tieszen, L. L., Baldocchi, D., et al. (2007). Deriving a light use efficiency model from eddy covariance flux data for predicting daily gross primary production across biomes. *Agricultural and Forest Meteorology*, *143*, 189–207.

- Zarco-Tejada, P. J., Berni, J. A. J., Suarez, L., Sepulcre-Cantó, G., Morales, F., & Miller, J. R. (2009). Imaging chlorophyll fluorescence with an airborne narrow-band multispectral camera for vegetation stress detection. *Remote Sensing of Environment*, 113, 1262–1275.
- Zhang, X., Friedl, M.A., Schaaf, C. B., Strahler, A. H., Hodges, J. C. F., Gao, F., et al. (2003). Monitoring vegetation phenology using MODIS. *Remote Sensing of Environment*, 84, 471–475.
- Zhang, Q., Middleton, E. M., Cheng, Y. -B., & Landis, D. R. (2013). Variations of foliage chlorophyll fAPAR and foliage non-chlorophyll fAPAR (fAPAR<sub>chl</sub>, fAPAR<sub>non-chl</sub>) at the Harvard Forest. *IEEE Journal of Selected Topics in Applied Earth Observations and Remote Sensing*, 6, 2254–2264.
- Zhang, Q., Middleton, E. M., Gao, B. C., & Cheng, Y. -B. (2012). Using EO-1 hyperion to simulate HypsIRI products for a coniferous forest: The fraction of PAR absorbed by chlorophyll (fAPAR<sub>chl</sub>) and Leaf Water Content (LWC). *IEEE Transactions on Geoscience and Remote Sensing*, 50, 1844–1852.
- Zhang, Q., Middleton, E. M., Margolis, H. A., Drolet, G. G., Barr, A. A., & Black, T. A. (2009). Can a satellite-derived estimate of the fraction of PAR absorbed by chlorophyll (fAPAR<sub>chl</sub>) improve predictions of light-use efficiency and ecosystem photosynthesis for a boreal aspen forest? *Remote Sensing of Environment*, 113, 880–888. <http://dx.doi.org/10.1016/j.rse.2009.01.002>.
- Zhang, Q., Xiao, X., Braswell, B., Linder, E., Baret, F., & Moore, B. (2005). Estimating light absorption by chlorophyll, leaf and canopy in a deciduous broadleaf forest using MODIS data and a radiative transfer model. *Remote Sensing of Environment*, 99, 357–371.
- Zhang, Q., Xiao, X., Braswell, B., Linder, E., Ollinger, S., Smith, M. -L., et al. (2006). Characterization of seasonal variation of forest canopy in a temperate deciduous broadleaf forest, using daily MODIS data. *Remote Sensing of Environment*, 105, 189–203.
- Zhou, L., Tucker, C. J., Kaufmann, R. K., Slayback, D., Shabanov, N. V., & Myneni, R. B. (2001). Variations in northern vegetation activity inferred from satellite data of vegetation index during 1981 to 1999. *Journal of Geophysical Research*, 106, 20,069–20,083. <http://dx.doi.org/10.1029/2000JD000115>.